Limnol. Oceanogr., 57(3), 2012, 809–825

doi:10.4319/lo.2012.57.3.0809

The influence of pore-water advection, benthic photosynthesis, and respiration on calcium carbonate dynamics in reef sands

Alexandra M. F. Rao,[a,1,*] Lubos Polerecky,[a] Danny Ionescu,[a] Filip J. R. Meysman,[b,c] and Dirk de Beer [a]

[a] Max Planck Institute for Marine Microbiology, Bremen, Germany
[b] Centre for Estuarine and Marine Ecology (CEME), Royal Netherlands Institute for Sea Research (NIOZ), Yerseke, The Netherlands
[c] Laboratory of Analytical and Environmental Chemistry, Earth System Science Research Unit, Vrije Universiteit Brussel (VUB), Brussels, Belgium

Abstract

To investigate diel calcium carbonate ($CaCO_3$) dynamics in permeable coral reef sands, we measured pore-water profiles and fluxes of oxygen (O_2), nutrients, pH, calcium (Ca^{2+}), and alkalinity (TA) across the sediment–water interface in sands of different permeability at Heron Reef, Australia. Background flushing rates were high, most likely as a result of infaunal burrow irrigation, but flux chamber stirring enhanced pore-water exchange. Light and pore-water advection fueled high rates of benthic primary production and calcification in sunlit surface sediments. In the light, benthic photosynthesis and calcification induced surface minima in Ca^{2+} and TA and peaks in pH and O_2. Oxygen penetration depth in coarse sands decreased from ~ 1.2 cm during the day to ~ 0.6 cm at night. Total oxygen uptake (TOU) in dark chambers was three to fourteen times greater than diffusive uptake and showed a direct effect of pore-water advection. Greater sediment oxygen consumption rates were observed in higher permeability sands. In the dark, TA release was not stimulated by increasing TOU because of a damping effect of pore-water advection on metabolic $CaCO_3$ dissolution efficiency. On a daily basis, $CaCO_3$ undergoes net dissolution in Heron Reef sands. However, pore-water advection can reverse the $CaCO_3$ budget and promote $CaCO_3$ preservation under the most energetic conditions.

Anthropogenic release of CO_2 to the atmosphere leads to ocean acidification, which is predicted to have a strong adverse effect on marine ecosystems (Guinotte and Fabry 2008). On 100 to 1000–yr timescales, perturbations in the oceanic CO_2 inventory are increasingly buffered by the large stock of calcium carbonate ($CaCO_3$) in surface sediments, which plays an important role in the ocean carbon cycle (Broecker and Peng 1987). This stabilizing feedback on ocean alkalinity and pH is known as $CaCO_3$ compensation. In essence, the lower carbonate ion (CO_3^{2-}) concentrations that result from acidification are compensated by more dissolution, and hence less preservation, of $CaCO_3$ in marine sediments. Therefore, an in-depth understanding of sedimentary $CaCO_3$ dissolution is essential to predicting the fate of fossil-fuel CO_2 and the long-term evolution of ocean acidification (Boudreau et al. 2010).

The dissolution or preservation of $CaCO_3$ in ocean sediments is mainly controlled by the saturation state of bottom water, which decreases with water depth as a result of the combined effects of the biological pump and the pressure and temperature dependence of $CaCO_3$ solubility. Below the calcite and aragonite saturation horizons, these carbonate phases readily dissolve, leading to less $CaCO_3$ preservation in deep-sea sediments. However, bottom water undersaturation is not the only driver of sedimentary carbonate dissolution. It has been estimated that up to 50% of sedimentary $CaCO_3$ dissolution occurs in sediments above the calcite saturation horizon (Archer 1996), in which metabolic CO_2 production and the oxidation of reduced metabolites can induce pore-water undersaturation and thereby fuel metabolic or respiration-driven dissolution. Most studies of metabolic $CaCO_3$ dissolution have been conducted in deep-sea environments (Jahnke and Jahnke 2004; Martin and Sayles 2006). While studies in shallow environments have mainly focused on fine-grained sediments (Alongi et al. 2006), metabolic carbonate dissolution may also be important in permeable carbonate sands (Burdige and Zimmerman 2002), which present several contrasts to more organic-rich, finer-grained deposits. Solute exchange in muddy sediments is primarily driven by molecular diffusion and macrofaunal activity, while the high permeabilities of sandy deposits permit pore-water transport by advection and dispersion (Huettel and Webster 2001). Pore-water flow in permeable sediments is linked to pressure gradients associated with current–topography interactions, wave pumping, groundwater discharge, temperature and salinity gradients, as well as macrofaunal activity.

In recent years, increasing attention has been focused on the biogeochemistry of permeable sands because of the areal significance of these sediments on continental shelves worldwide (Emery 1968), the large contribution (30–50%) of continental margins to global marine primary production (Walsh 1991), the efficient export of organic matter to sediments in ocean margins (Jahnke 1996), and the high

* Corresponding author: alexandra.rao@nioz.nl

[1] Present address: Laboratory of Analytical and Environmental Chemistry, Earth System Science Research Unit, Vrije Universiteit Brussel (VUB), Brussels, Belgium

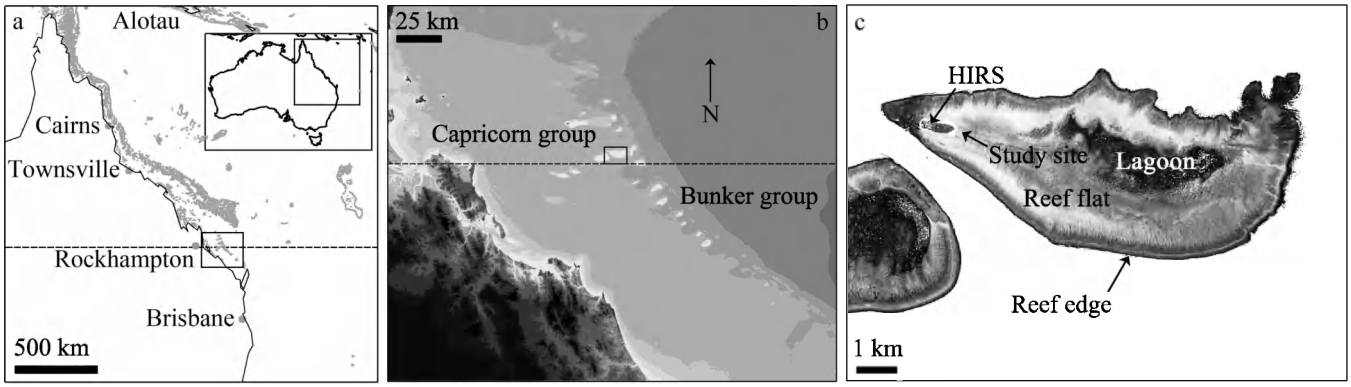

Fig. 1. Map of (a) the Australian Great Barrier Reef, (b) the Capricorn–Bunker Island group, and (c) the Shark Bay study site at Heron Reef. HIRS represents the Heron Island Research Station. The dashed line is the Tropic of Capricorn.

metabolic activity characteristic of permeable sands (Huettel and Webster 2001). These factors indicate that sandy deposits, such as carbonate reef sands, play an important role in carbon and nutrient cycling in ocean margins. A large part (> 20%) of the global ocean carbonate accumulation occurs in coral reefs (Milliman and Droxler 1996). Furthermore, reef environments are characterized by high gross primary production rates, which are supported by the recycling of nutrients and organic matter from coral mucus, eggs, and phyto- and zooplankton detritus in reef sands (Wild et al. 2004; Werner et al. 2006). As biogenic carbonate sands have greater specific surface area, porosity, permeability, and buffering capacity than silicate sands, they may also support higher metabolic rates, more biofilm formation, greater bacterial abundance, different microbial populations, and a stronger response to organic substrates than terrestrially derived silicate sands (Wild et al. 2005). Therefore, $CaCO_3$ and organic matter cycling in reef sands present a new challenge to understanding the global carbon (C) cycle and ecosystem dynamics in fragile coral reef environments.

With this in mind, the objective of the present study was to develop a mechanistic understanding of the influence of physically induced advective pore-water transport on metabolic carbonate dissolution and $CaCO_3$ dynamics in biogenic carbonate sands.

$$Ca^{2+} + 2HCO_3^- \rightleftarrows CaCO_3 + H_2O + CO_2\uparrow \qquad (1)$$

An accurate interpretation of the link between benthic $CaCO_3$ dynamics and pore-water exchange requires consideration of microalgal CO_2 uptake in surface sediments and the production of metabolic acidity by microbial respiration below the surface layer, which promote calcification and $CaCO_3$ dissolution (Eq. 1), respectively, in reef sediments (Werner et al. 2008; Schoon et al. 2010; Santos et al. 2011). Direct measurements of sediment organic carbon and $CaCO_3$ turnover rates were obtained using stirred flux chamber incubations to quantify benthic solute fluxes over a range of pore-water exchange rates. Trends in measured fluxes are interpreted in the context of planar optode measurements of sediment community respiration and pore-water solute profiles measured in the presence (in situ) and absence (ex situ) of advection to unravel the interconnected roles of benthic photosynthesis, respiration, and pore-water exchange on $CaCO_3$ dynamics.

Methods

Study site—Sampling was conducted in April 2010 in Shark Bay at Heron Reef (Fig. 1), a lagoonal platform reef system at the southern boundary of the Great Barrier Reef, Australia (23°26′37″S, 151°55′08″E). During the 2-week sampling campaign, tidal range varied from 0.5 m at neap tide to 2 m at spring tide, with water temperature ranging from 22°C to 30°C and salinity ranging between 35.24 and 35.87. Two subtidal sites were selected (Table 1), one about 20 m from the low tide line (coarse sand, CS) and another on the edge of the reef flat, among coral patches (fine sand, FS). Water depth at these sites ranged from 20 cm at low tide to 2 m at high tide. Heron Reef sands are generally low in organic carbon (0.24%) and nitrogen (0.042%) content (Wild et al. 2004). We were careful to avoid sampling in areas with a high density of macrofaunal structures. However, the sediment community at Heron Reef is known

Table 1. Sediment properties at CS and FS sites. Results represent the mean ± 1 SD.

Site	Coarse sand	Fine sand
Porosity	0.44±0.02(n=5)	0.45±0.01(n=5)
Permeability ($\times 10^{-11}$ m^2)	7.4±3.6(n=5)	0.7±0.4(n=2)
Grain size (μm)	897±53(n=3)	590±35(n=3)
Specific surface area (<1 mm, m^2 g^{-1})	0.73±0.11(n=10)	1.48±0.08(n=10)
Aragonite (wt %)	70±3(n=10)	74±3(n=10)
Low-Mg calcite (<4 mol % Mg, wt %)	3.7±0.4(n=10)	3.9±0.6(n=10)
High-Mg calcite (>4 mol % Mg, wt %)	26±3(n=10)	22±3(n=10)

to include abundant benthic microalgae (diatoms, dinoflagellates, cyanobacteria, and coralline algae) and macrofauna, including mud shrimps (*Callianassa* sp.), polychaetes, nematodes, and gastropods (Werner et al. 2006, 2008; Logan et al. 2008).

Ex situ planar optode imaging of oxygen consumption rates—The flow-through method of Polerecky et al. (2005) was used to measure potential sediment oxygen consumption rates (OCR) with high spatial resolution in two dimensions (2D). Sediment cores were collected in core liners equipped with a planar oxygen optode on one side and returned to the laboratory for analysis within 6 h at in situ temperature. After percolating intact sediment cores for 2–3 min with aerated seawater, the percolation was stopped and 2D images of pore-water oxygen concentrations were determined using the luminescence lifetime imaging system (Holst and Grunwald 2001). Optodes were calibrated using recordings in air-saturated overlying water and in anoxic sediment at depth. For every pixel, the initial slope of the measured decrease in oxygen (O_2) was multiplied by sediment porosity to obtain an image of OCR expressed per unit volume of sediment. Each OCR image was aligned such that the sediment surface was horizontal and was horizontally averaged at 2-mm depth intervals to obtain one-dimensional depth profiles.

In situ flux chamber incubations—Fluxes of solutes across the sediment–water interface (SWI) were measured with in situ benthic flux chambers previously described by Janssen et al. (2005). Acrylic flux chamber cylinders (20-cm inner diameter [i.d.]) were implanted 20 cm into the sediment, enclosing 15–20 cm of overlying water. Advective pore-water exchange was maintained within the enclosed sediments by acrylic plates suspended 10 cm above the SWI, which stirred the overlying water continuously. We report results from 36 chamber incubations, including three replicate light and dark incubations conducted at three different stirring rates at sites CS and FS. Stirring rates were chosen to represent a range of interfacial pressure gradients and solute exchange conditions, from less than 0.25 Pa with diffusion-dominated transport and minimal pore-water advection (10 rotations per minute [rpm]) to strong advective transport (40 and 60 rpm) after Janssen et al. (2005). Laboratory experiments have shown that a stirring rate of 40 rpm produces moderate pore-water advection in response to an interfacial pressure gradient similar to that previously measured at 10-mm–high mounds exposed to unidirectional flow of 20 cm s^{-1} at 10 cm above the bed (Janssen et al. 2005).

After flux chamber lids were secured at the start of incubations, a sodium bromide tracer was added to the overlying water to a final concentration of 3–5 mmol L^{-1}. Samples of overlying water (~ 50 mL) were collected hourly from each chamber for solute analyses as described below. Samples were collected in plastic syringes for nutrient, bromide (Br^-), Ca^{2+}, pH, and total alkalinity (TA) analyses and in glass syringes for O_2 analyses. Most likely as a result of undiluted tracer solution remaining in the injection port, initial (time zero) Ca^{2+} and Br^- measurements were anomalous and are therefore not considered in the final analysis.

Flux chamber incubations were conducted around midday for an average of 5 h. During each set of flux chamber incubations we monitored surface-water temperature, collected water samples for salinity, and continuously recorded the incident flux of photosynthetically active radiation (PAR) adjacent to the flux chambers using submersible light loggers (Odyssey). Continuous measurements of dissolved O_2 in chamber water were made with fiber optodes mounted through chamber lids as described by Janssen et al. (2005). Optode results were calibrated with measurements of dissolved O_2 in discrete hourly samples by membrane inlet mass spectrometry (MIMS).

The dilution of Br^- tracer was used to quantify the volume of overlying water and the rate of pore-water filtration in each flux chamber. Effective chamber volume and height were determined from the known chamber diameter, the known volume and concentration of Br^- tracer injected at the start of incubations, and the initial chamber concentration of Br^- in excess of natural seawater Br^- (ex Br^-), obtained by extrapolating the measured ex Br^- to the start of the incubation using linear regression. The slope of this regression was used to estimate pore-water filtration rate from the dilution of chamber water ex Br^- with pore water containing no excess Br^-. Benthic solute fluxes were subsequently determined from the chamber height and the slope of linear regressions of chamber solute concentrations vs. incubation time.

As incubation time progresses, the buildup or consumption of overlying water solutes and associated changes in solute concentration gradients at the SWI within flux chambers may alter measured solute fluxes to a degree (Bender et al. 1989; Reimers et al. 2001). In the case of Br^- tracer, the mixing of Br^- into surface sediments results in smaller interfacial gradients and a decline in Br^- influx during incubations, raising potential concerns regarding estimates of initial tracer concentrations and fluxes resulting from linear fits to chamber Br^- time series. Nevertheless, detailed hydrodynamic investigations of this flux chamber design have indicated that tracers and other solutes such as O_2 exhibit a nearly linear change in chamber water concentration with time at a range of stirring rates in permeable sediment (Janssen et al. 2005). These results demonstrate that solute fluxes in these stirred chambers remain fairly constant over 2–6-h incubations in advection-dominated environments, as has been confirmed in this study.

In principle, chamber solute fluxes should be corrected for dilution with bottom water at each sample collection, but since the loss of Br^- tracer during deployments was generally low (14% ± 6%) and since previous chamber studies (Bender et al. 1989; Jahnke and Jahnke 2000; Reimers et al. 2001) have shown that this dilution error is likely offset by uncertainties due to changing chamber water solute concentrations and interfacial pore-water gradients during chamber incubations, this correction has been ignored. Hourly solute fluxes from light and dark chambers have been scaled to a per-day basis by integrating over the monthly and annual mean number of hours of daylight and darkness obtained from records of the

Australian Government Bureau of Meteorology (BOM, http://www.bom.gov.au/climate/averages/tables/cw_039122.shtml).

Microsensor profiling—In situ pore-water O_2 and pH profiles were measured with Clark-type and liquid ion-exchange microsensors mounted on an autonomous profiling instrument, as described in Glud et al. (1999). The microsensors were thick-walled, with tip diameters of 200–300 μm, inner sensing diameters of approximately 5 μm (O_2) and 20 μm (pH), and 90% response times of less than 5 s (O_2) and 1 s (pH). The profiling instrument was placed on the sediment with the microsensors initially positioned 2–3 cm above the sediment surface. Profiles were measured every hour over a 24-h period to a sediment depth of 6–8 cm at intervals of 0.5 mm. Dark microprofiles are available in FS, and both light and dark profiles are available in CS.

Microsensors were also used ex situ to characterize the activity of microphytobenthos and their influence on pore-water chemistry (O_2 and pH) in the top few millimeters of sediment under a diffusion-dominated solute exchange regime. One sediment core from each site was collected and analyzed in the laboratory within 10 h at in situ temperature, as previously described (Polerecky et al. 2007). Steady-state O_2 microprofiles (n = 4–5) were measured at incident light intensities ranging from 0 to 5.26 mol photons m^{-2} h^{-1}. In the same cores, steady-state pH profiles (n = 3) were measured in the dark and at saturating light intensity.

Diffusive O_2 fluxes, J, were calculated from O_2 microprofiles as

$$J = -\mathrm{Do}_2 \frac{\partial[\mathrm{O}_2]}{\mathrm{dz}} \quad (2)$$

where z is depth and $[O_2]$ denotes O_2 concentration. Ex situ profiles measured under diffusive conditions were used to calculate O_2 fluxes at the diffusive boundary layer (J_{DBL}) and at the bottom of the euphotic surface layer (J_{EUPH}). Concentration gradients at the DBL and the temperature- and salinity-dependent molecular diffusion coefficient of O_2 in seawater (Do_2; Li and Gregory 1974) were used to determine J_{DBL}. To calculate J_{EUPH}, pore-water O_2 concentration gradients at the base of the euphotic layer were adjusted for porosity ($\times\varphi$), and Do_2 was corrected for sediment tortuosity ($D^* = Do_2/\theta^2$), according to Archie's Law ($\theta^2 = \varphi^{1-m}$, with m = 2 for sands; Boudreau 1997). The euphotic zone thickness (z_{EUPH}) was estimated as the depth at which net O_2 production at saturating light intensities changes to net consumption. Diffusive oxygen uptake (DOU) rates were calculated as J_{DBL} in dark microprofiles. Net primary production (NPP) by benthic photosynthesis in the light under diffusive conditions was calculated as the sum of upward and downward diffusive fluxes in the euphotic layer ($NPP = J_{EUPH} - J_{DBL}$) and gross photosynthesis (GPP) at a given light intensity E as $GPP(E) = J_{EUPH}(E) - J_{DBL}(E) + J_{DBL}(0)$, assuming that light respiration is equal to dark respiration, given by $J_{DBL}(0)$. A saturating exponential model, $J = J_0 + J_{max}[1 - \exp(-E/E_k)]$, was fitted to J_{DBL} to estimate the light acclimation intensity, E_k (Webb et al. 1974). Net benthic photosynthesis and DOU derived from diffusive fluxes were subsequently compared to light- and dark-chamber O_2 fluxes measured under advective conditions.

In situ profiles were similarly used to calculate O_2 fluxes at the SWI (J_{SWI}) using the tortuosity-corrected effective diffusivity, D^*, and concentration gradients at the SWI. In situ rates of net and gross photosynthesis in the daytime were calculated as $NPP = J_{EUPH} - J_{SWI}$ and $GPP = NPP + J_{SWI}(0)$, assuming that daytime respiration is equal to nighttime respiration, given by $J_{SWI}(0)$.

Pore-water and sediment sampling—Sediment cores for solid-phase and pore-water samples were collected at each site using acrylic core barrels (5-cm i.d.), pistons, and rubber stoppers. For pore-water sampling, core barrels were drilled at 1-cm depth intervals with 0.25-cm septae, which were taped shut during core collection and immediately fitted with Rhizon pore-water samplers following core retrieval (Seeberg-Elverfeldt et al. 2005). Samples from each Rhizon sampler were limited to 3–3.5 mL at each depth interval and were collected consecutively from the interface downcore using 5-mL plastic syringes for nutrient, Ca^{2+}, pH, and TA analyses. Cores collected with intact (undrilled) core barrels were extruded and sliced at 1-cm intervals for porosity, grain size, sediment specific surface area (SSA), and crystallinity analyses. Intact cores of 3.6-cm i.d. were also used for falling head permeametry.

Analytical methods—Sediment samples were analyzed for SSA on a Quantachrome NOVA 3000 surface area analyzer with a 10-point Brunauer Emmett Teller method. Porosity was measured gravimetrically, and grain size was measured on a sieve column at intervals of 0.5 ϕ, agitated for 15 min with a Retsch AS200 sieve shaker. $CaCO_3$ crystallinity was analyzed by x-ray diffraction (XRD) on a Bruker D8-Advance diffractometer with CuKα radiation at the University of Liège, Belgium. Sediment samples were carefully ground and homogenized to avoid a grain size bias (Mélières 1978). Ten powdered sediment samples from each site were mounted as unoriented powder by the back-side method (Brindley and Brown 1980) and submitted to XRD between 2° and 45° 2θ. The data were analyzed in a semi-quantitative way following Cook et al. (1975). The intensity of the 3.39-Å, 3.03-Å, and 3.00-Å peaks were used to estimate the mineral fractions of aragonite, low-magnesium (Mg) calcite (LMC), and high-magnesium calcite (HMC). The distinction between LMC and HMC was made using the measured effect of Mg substitution on calcite crystal lattice spacing (Milliman 1974) and assuming the common classification of HMC (> 4 mol % Mg), following the method of Flügel (2004).

For chlorophyll *a* (Chl *a*) extraction, three fresh sediment cores were collected from each site and subsampled in 1-cm depth intervals a few minutes after collection. Wet homogenized sediment (3–5 g) from each subsample was poured into preweighed vials, 8 mL of solvent (methanol and acetone at a 1 : 1 volume ratio) was added to each vial, and samples were vigorously shaken and stored for 10 h at 4°C in the dark. After this extraction step, samples were centrifuged (4670 *g* for 3 min at 10°C), and

the absorbance spectra of the supernatant were measured in a standard cuvette with a spectrometer (Ocean Optics, USB2000). Based on a calibration with Chl *a* standards, supernatant Chl *a* concentrations were calculated following Lorenzen (1967) as Chl *a* (mg L^{-1}) = 70.55 ($A_{664} - A_{710}$), where A_λ is absorbance at wavelength λ. Finally, wet sediment Chl *a* contents were converted to μg (g dry sediment)$^{-1}$ after correction for sediment water content.

Once recovered, pore-water and chamber water samples were immediately analyzed for pH using an Orion ROSS glass electrode, calibrated with NBS buffers. Water samples for Br^-, Ca^{2+}, TA, and nutrients were subsequently filtered (Sartorius 0.2-μm regenerated cellulose syringe filters) and refrigerated until analysis. In the laboratory, water samples were analyzed colorimetrically for Br^- (coefficient of variation [CV] 0.74%, averaged over 16 replicate measurements of standards) following the method of Presley (1971). Phosphate, silicate, total nitrate ($NO_3^- + NO_2^-$), and ammonium were measured manually using scaled-down standard colorimetric methods (Strickland and Parsons 1972) to better than 0.2 μmol L^{-1} (ΣNO_3^-, PO_4^{3-}, and NH_4^+) and 0.4 μmol L^{-1} (Si) precision. Total dissolved sulfide ($\sum H_2S$) was measured in pore-water samples following the Cline (1969) method to better than 2 μmol L^{-1} precision. Salinity in surface water samples was measured using a laboratory conductivity sensor (Radiometer Analytical). Alkalinity (± 0.2%) and calcium (± 0.1%) were measured by manual scaled-down Gran and ethylene glycol tetraacetic acid (EGTA) titrations (Tsunogai et al. 1968) using an ultraprecision micrometer burette (Roger Gilmont Instruments). The analytical precision of EGTA titrations was improved by measuring the sample and > 90% of the titrant volume by weight prior to the start of each titration. The saturation index of pore water with respect to aragonite (Ω_a) was calculated from pH and TA using the carbonate and borate dissociation constants of Dickson (1990) and Mehrbach et al. (1973), as reinterpolated by Dickson and Millero (1987). Here, Ω_a refers to the ratio of the ion concentration product $[Ca^{2+}]$ $[CO_3^{2-}]$ to the solubility product of aragonite, after Mucci (1983).

Water samples for discrete O_2 analyses were collected in glass syringes and filled into 5-mL gas-tight Exetainer vials with screw caps and preserved with 200 μL of 50% $ZnCl_2$. Sample vials were filled from the bottom with a 2–3-mL overflow volume to prevent exchange with atmospheric O_2. Samples were stored refrigerated and underwater to avoid bubble formation and were analyzed by MIMS within 6 weeks of collection (GAM 200 InProcess Instruments; Kana et al. 1994). Dissolved gas concentrations were determined from MIMS analyses using the solubility constants of Weiss (1970). Average precision (O_2:Ar CV 0.21%) was calculated from replicate (n = 15) measurements of an air-saturated standard.

Statistical analyses—In general, results are reported as the mean ± 1 standard deviation (SD) of n replicate measurements. Nonparametric statistics were used in the interpretation of results, including the Mann–Whitney U-test for comparison of means of two independent groups of measurements, the Wilcoxon rank sum test for comparison of the mean of a sample of repeated measurements with a hypothetical mean value, and Spearman's rank correlation as a measure of the statistical dependence between two variables. Outliers in the data set were identified using Grubb's outlier test for one outlier in small samples. Multivariate correlations were analyzed using multiple regression analysis with backward elimination of independent variables based on comparisons of standardized partial regression coefficients (β) and Pearson's correlation coefficient (R). Statistical analyses were conducted in the open-source programming language R using the *stats* extension package.

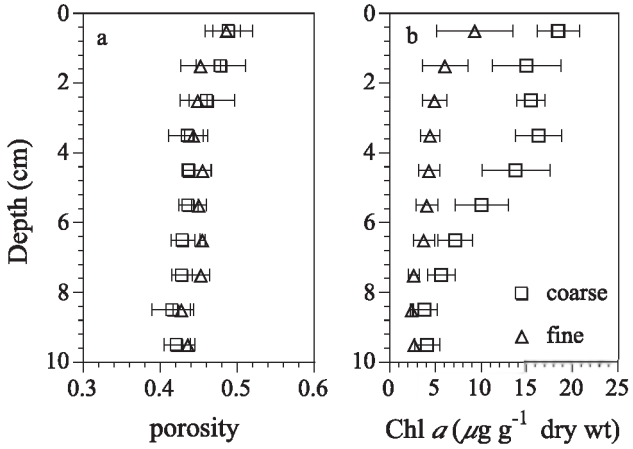

Fig. 2. (a) Porosity and (b) chlorophyll *a* content in Heron Reef sediments (mean ± 1 SD, n = 3). Dry wt refers to dry weight.

Results

Sediment properties—Sediments at sites CS and FS have similar porosity and $CaCO_3$ composition, but sands at CS are significantly coarser (Mann–Whitney; $p = 0.05$), more permeable (Mann–Whitney; $p < 0.05$), and richer in Chl *a* (Mann–Whitney; $p < 0.001$) than those at site FS (Table 1). Porosity profiles are very similar at both sites, showing a small decrease with depth from 0.5 at the surface to 0.44 at 10-cm depth (Fig. 2a). Sediment Chl *a* content at both sites was highest in the top 1-cm layer, gradually decreased with depth, and was detectable down to 10-cm depth (Fig. 2b). In the upper 6 cm of sediment, Chl *a* content was about three times higher in CS than in FS. By 9–10-cm depth, sediment Chl *a* content was similar at both sites. The instantaneous PAR flux at the SWI often exceeded 3 mol photons m^{-2} h^{-1} around midday (Fig. 3). Sediment PAR exposure integrated over the chamber incubation time ranged from 7.6 to 12.1 mol photons m^{-2} (Table 2).

Ex situ planar optode imaging of oxygen consumption rates—OCRs in CS were roughly twice as high as in FS (Fig. 4). This difference is only significant in the upper 3.5 cm of sediment (Mann–Whitney; $p < 0.05$) as a result of the greater OCR variability in deeper layers in FS. The OCR in CS exhibited greater horizontal variability within cores (compare filled symbols in Fig. 4a) as well as between replicate cores (compare error bars in Fig. 4a) than in fine

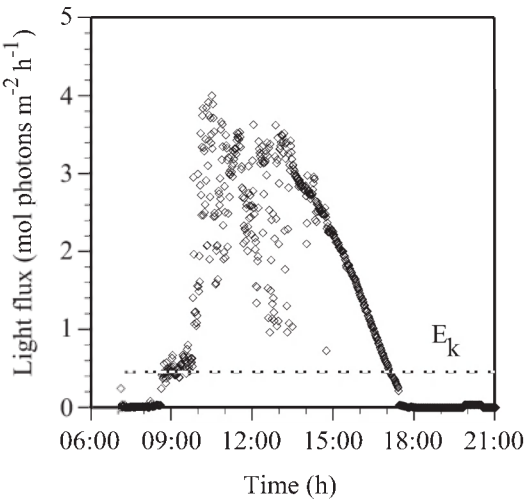

Fig. 3. An example time series of benthic light flux (04 April 2010) at Heron Reef. Dotted line represents the light acclimation intensity (E_k) measured in the laboratory under diffusive stirring conditions (Table 4).

sediments. No significant vertical trends were observed in OCR profiles.

Benthic flux chamber incubations—Representative examples of time-series results for light- and dark-chamber incubations are presented in Fig. 5. In general, ex Br^- decreased linearly with time. Pore-water exchange rates in flux chamber incubations (Table 2), derived from the rate of change in chamber water ex Br^-, range from 74 ± 32 L m^{-2} d^{-1} in FS to 128 ± 14 L m^{-2} d^{-1} in CS at the highest stirring rate. Exchange rates in CS were significantly higher than in FS at all stirring rates (Mann–Whitney; $p < 0.01$). Stirring significantly enhanced pore-water exchange in CS (Spearman; $p = 0.03$), but not in FS (Spearman; $p = 0.60$).

Similar trends in chamber water O_2 are evident in discrete MIMS samples and continuous optode measurements, although the latter are not available for all incubations (Fig. 5). Benthic O_2 fluxes derived from the analysis of discrete samples are not significantly different from those calculated from continuous optode measurements (Mann–Whitney; $p = 0.93$; Table 3). Therefore, for comparison with benthic flux estimates of other solutes, the subsequent discussion will be based on chamber O_2 fluxes derived from discrete samples.

Table 2. Summary of filtration rate and sediment PAR exposure measured during each set of flux chamber incubations (mean ± 1 SD). Chamber sets are denoted by sampling site (CS and FS) and flux chamber stirring rate (10, 40, and 60 rpm). Filtration rates for each chamber set are averaged over all light and dark chambers. Sediment PAR flux is integrated over the incubation time of three replicate light-chamber incubations.

	Filtration rate (L m^{-2} d^{-1}), n=6	PAR exposure (mol photons m^{-2}), n=3
CS 10 rpm	103±30	12.12±1.12
CS 40 rpm	118±44	12.01±0.54
CS 60 rpm	128±14	7.71±0.93
FS 10 rpm	90±28	12.04±1.97
FS 40 rpm	74±32	9.68±0.55
FS 60 rpm	98±68	7.59±0.71

A linear decline in O_2 concentrations was observed in all dark-chamber incubations (Fig. 5). The rate of decline in dark-chamber O_2 represents a measure of total oxygen uptake (TOU), which ranges from 0.73 mmol m^{-2} h^{-1} at the 'non-advective' setting (10 rpm) in FS to 2.67 mmol m^{-2} h^{-1} at the highest advective setting (60 rpm) in CS. A significant increase in TOU was observed with increasing pore-water exchange (Spearman; $p < 0.001$). Furthermore, TOU in CS was greater than in FS (Mann–Whitney; $p < 0.001$; Table 3). In the presence of light, chamber O_2 concentrations increased in response to photosynthesis by benthic microalgae (Fig. 5). In most light chambers, the rate of O_2 evolution decreased toward the end of incubations, and therefore O_2 time series were not perfectly linear. This can be explained by the decrease in PAR flux in the afternoon (Fig. 3), which is presumably accompanied by falling benthic photosynthesis rates. For comparison with benthic flux estimates of other solutes, however, NPP has been estimated from the slope of linear regressions of all light-chamber O_2 results, and GPP rates are calculated as the difference between NPP and mean dark-chamber TOU.

Despite significant metabolic activity, nutrient concentrations remained low throughout all incubations (data not shown). Generally, nitrate, ammonium, and phosphate concentrations in chamber water were below 1 μmol L^{-1}, silicate concentrations remained below 2 μmol L^{-1}, and calculated benthic nutrient fluxes were near zero.

A decrease in dark-chamber pH and an increase in light-chamber pH during incubations are expected as a result of sediment community respiration and NPP, respectively. In general, the observed trends in chamber-water pH are consistent with these effects (Fig. 5). As discussed later, benthic photosynthesis and respiration alter the $CaCO_3$ saturation state in sediment pore water, resulting in the precipitation and dissolution of $CaCO_3$. Measured calcium and alkalinity fluxes indicate net $CaCO_3$ precipitation in light chambers and dissolution in dark chambers (Fig. 5; Table 3). In the following discussion, we address the processes controlling the balance between sediment calcification and dissolution.

Pore-water profiles—Examples of in situ microprofiles of O_2, pH, and Ω_a in Heron Reef sands are presented in Fig. 6. Benthic photosynthesis in sunlit surface sediments promotes O_2 evolution and CO_2 uptake, resulting in coincident peaks in O_2, pH, and Ω_a at 1–2 mm depth. In deeper sediments, pore-water O_2, pH, and Ω_a decline as a result of O_2 consumption and CO_2 release associated with organic matter oxidation. As a result of benthic photosynthesis, O_2 penetration in CS was twice as deep in the light as in the dark (Table 4). No significant difference was observed between nighttime oxygen penetration depth (OPD) in CS and FS. Benthic primary production rates calculated from daytime O_2 microprofiles in CS and DOU calculated from nighttime profiles in both CS and FS were

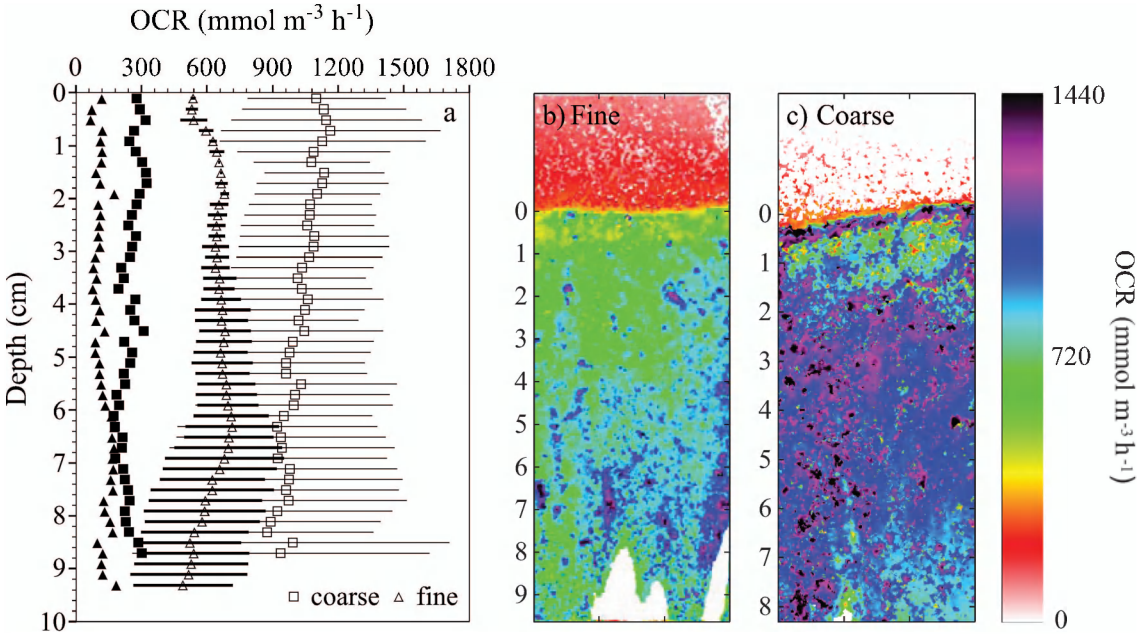

Fig. 4. (a) Depth profiles of potential sediment oxygen consumption rates (OCRs) in Heron Reef sediments. Open symbols represent the mean ± 1 SD of measurements in replicate cores, respectively, whereas filled symbols depict the horizontal variability (± 1 SD) of OCR within cores ($n = 6$ and $n = 2$ in coarse and fine sand, respectively). Examples of 2D OCR images are shown in (b) fine sand and (c) coarse sand. (b) The white areas at the bottom of the image correspond to sediment regions in which OCR was not determined as a result of lack of O_2 during the measurement. (b, c) OCR values in black areas are ≥ 1440 mmol m^{-3} h^{-1}.

very low, with a high spatial variability. Note, however, that these calculations only capture the diffusive component, and not the advective component, of benthic O_2 fluxes.

Under diffusive conditions in the laboratory, OPD was considerably shallower than in situ, both under illumination and in the dark (Fig. 7). Laboratory OPD was slightly shallower in CS than in FS in the dark, whereas it was similar at both sites under saturating illumination (Table 4). Peak O_2 concentrations under illumination were greatly enhanced in the laboratory under diffusive conditions, relative to peak in situ concentrations. At a given

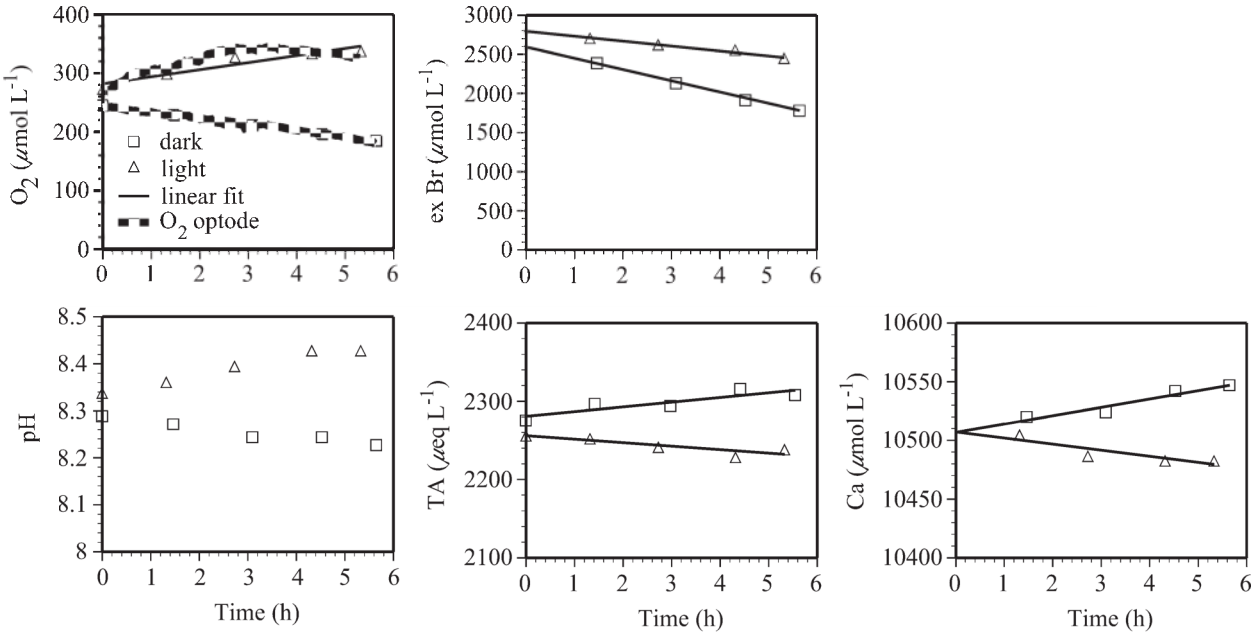

Fig. 5. Time series results for oxygen, excess bromide, pH, alkalinity, and calcium in example light- and dark-chamber incubations. Linear trends (solid lines) were used to estimate benthic fluxes for all solutes except pH, as summarized in Table 3. Continuous chamber O_2 measurements (O_2 optode, thick broken line) are shown for comparison.

Table 3. Summary of flux estimates (mean ± 1 SD) from replicate in situ benthic flux chamber incubations in CS and FS sites at flux chamber stirring rates of 10, 40, and 60 rpm. Fluxes directed into the sediment are negative.

mmol m^{-2} h^{-1}	O_2 (MIMS), $n=3$	O_2 (optode)	TA, $n=3$	Calcium, $n=3$
CS 10 rpm				
Dark	−1.51±0.20	−1.51±0.15($n=2$)	1.67±0.50	1.16±0.22
Light	2.64±0.51	2.75($n=1$)	−2.27±0.32	−0.90±0.30
CS 40 rpm				
Dark	−2.24±0.32	−2.49±0.15($n=2$)	1.42±0.40	0.66±0.23
Light	4.19±0.54	4.57±0.26($n=2$)	−2.63±0.48	−0.71±0.31
CS 60 rpm				
Dark	−2.58±0.10		0.54±0.80	0.34±0.36
Light	1.93±0.44		−1.73±0.95	−0.78±0.32
FS 10 rpm				
Dark	−0.87±0.13	−0.73±0.18($n=2$)	1.04±0.50	0.62±0.23
Light	3.19±0.12	3.40±0.53($n=2$)	−1.55±0.48	−0.43±0.05
FS 40 rpm				
Dark	−1.10±0.35	−1.18±0.49($n=2$)	2.09±0.09	0.96±0.71
Light	2.16±0.35	3.19±0.51($n=2$)	−0.69±0.47	−0.34±0.12
FS 60 rpm				
Dark	−1.33±0.40	−1.50±0.39($n=2$)	1.04±0.50	0.54±0.60
Light	1.97±0.23	1.73±0.33($n=3$)	−0.67±0.24	−0.47±0.48

incident light intensity, peak O_2 concentrations as well as GPP and O_2 fluxes at the DBL (J_{DBL}) measured in the laboratory were on average higher in CS. The light acclimation intensity, E_k, was low and similar in both sites (Table 4). Changes in pore-water pH due to photosynthesis were more pronounced in surface sands under diffusive laboratory conditions than in situ. At the surface of larger sediment grains, pH increased up to 9–9.4 under saturating illumination in the laboratory. In comparison, in situ pore-water pH in the euphotic zone rose only to 8.3 (Table 4). At saturating illumination in the laboratory, peak pH values were similar in both sediment types (~ 8.45 at 1–1.5 mm depth), but in the dark pH decreased slightly more in CS (to 7.7) than in FS (to 7.81; Fig. 7).

The distributions of pore-water Ca^{2+}, TA, $\sum H_2S$, NH_4^+, and $Si(OH)_4$ measured in discrete pore-water samples from cores obtained in CS and FS are shown in Fig. 8. Measured concentrations of pore-water NO_3^- were generally less than 1 μmol L^{-1} at both sites (data not shown). These profiles demonstrate large spatial variability and small concentration gradients with depth, especially in CS. Ammonium and silicate, released in sediments by the remineralization of organic material, are more depleted in coarser sand. As a result of sulfate reduction, sulfide accumulates at depth to similar concentrations in CS and FS. Pore-water calcium and alkalinity distributions exhibit depletion by calcification in surface sediments and release at depth as a result of $CaCO_3$ dissolution and sulfate reduction. Trends in pore-water Ca^{2+} and TA profiles are more pronounced in finer sand.

Discussion

Advective pore-water exchange—Permeable coastal sediments have been compared to biocatalytic filters because of their importance as active sites of carbon, nutrient, and trace-metal cycling (Huettel and Webster 2001; Jahnke et al. 2005; Werner et al. 2006). While permeable sands are generally very low in organic content, the rapid advective supply of oxidants and particulate organic matter (POM) drives intense metabolic activity in these deposits (Jahnke et al. 2005; Rao et al. 2007).

The importance of advective pore-water exchange in Heron Reef sands is confirmed by the rapid exchange rates measured in our flux chamber incubations. However, it is important to recognize that pore-water exchange rates in FS and at low stirring (10 rpm) in CS (Table 2) were considerably higher than previous measurements in macrofauna-free sand of similar permeability (Janssen et al. 2005). These results indicate that background filtration rates in chamber incubations may have been enhanced by bioirrigation of infaunal burrows, which is independent of the imposed chamber stirring regime. Previous studies have estimated high rates of pore-water exchange due to burrow ventilation by burrowing shrimp *Callianassa* and *Upogebia* spp. (up to 11 L^{-1} d^{-1} for individual burrows and up to 110 L m^{-2} d^{-1} for natural populations; Forster and Graf 1995; Webb and Eyre 2004) and polychaetes *Arenicola* and *Diopatra* spp. (up to 4 L d^{-1} for individual burrows and up to 160 L m^{-2} d^{-1} for natural populations; Kristensen 2001). We suspect that macrofaunal activity was the dominant pore-water exchange mechanism in three incubations with the highest filtration rates, including one in each of the flux chamber sets FS 40 rpm (Grubb's outlier test; $p < 0.10$), FS 60 rpm (Grubb's outlier test; $p < 0.05$), and CS 40 rpm (Grubb's outlier test; $p < 0.10$). Because bioirrigation and physically induced pore-water exchange have different effects on O_2 (Huettel and Webster 2001; Kristensen 2001) and probably also $CaCO_3$ dynamics, the results of these chamber incubations must be cautiously interpreted.

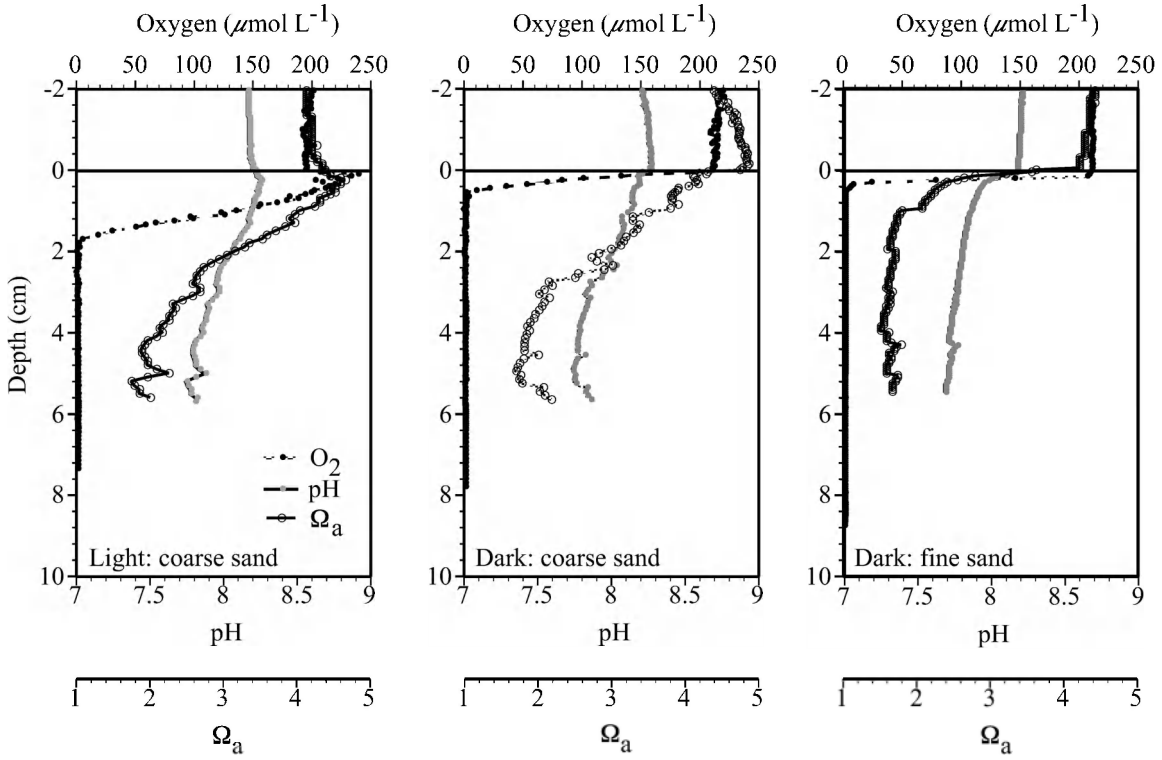

Fig. 6. Examples of in situ O_2, pH, and calculated Ω_a profiles in coarse and fine sand at Heron Reef in the light and dark.

In CS, filtration rates were significantly higher than in FS over all stirring rates (Mann–Whitney; $p < 0.01$), and an increase in filtration rate was observed with increased stirring (Spearman's; $p = 0.03$; Table 2). Filtration rates of ~ 125 L m^{-2} d^{-1}, measured at higher stirring rates (40 and 60 rpm), are in agreement with previous measurements using similar chambers in field and laboratory experiments (Glud et al. 1996; Janssen et al. 2005). Measured pore-water nutrient profiles (Fig. 8) and O_2 microprofiles (compare Figs. 6 and 7) also provide clear evidence of enhanced pore-water exchange, which modulates the buildup of daytime O_2 and pH peaks in euphotic surface sediments, increases the OPD, and prevents the accumulation of nutrients from organic matter decomposition,

Table 4. Summary of laboratory and in situ microsensor measurements. Laboratory results in the light represent measurements conducted under saturating light intensities (> 1 mol photons m^{-2} h^{-1}). Parameter calculations are explained in the text. The pH_{max} values marked with an asterisk were measured at the surface of large (1–2 mm) sand grains. Fluxes directed into the sediment are negative.

	Coarse		Fine	
	Dark	Light	Dark	Light
Ex situ microprofiles				
O_2 penetration depth (OPD, cm)	0.15–0.20	0.6–0.7	0.18–0.22	0.6–0.7
Euphotic zone thickness (z_{EUPH}, cm)	—	0.25–0.35	—	0.25–0.30
Peak [O_2] (μmol L^{-1})	—	697–895	—	498–697
J_{DBL} (mmol O_2 m^{-2} h^{-1})	−0.64±0.03	1.55±0.07	−0.56±0.05	0.92±0.07
GPP (mmol O_2 m^{-2} h^{-1})	—	2.79±0.10	—	1.83±0.09
E_k (mol photons m^{-2} h^{-1})	—	0.43±0.06	—	0.45±0.09
pH_{min}	7.72	7.72	7.83	7.83
pH_{max}	8.2	8.48(9.0–9.4)*	8.2	8.40–8.48
In situ microprofiles				
O_2 penetration depth (OPD, cm)	0.3–1.2	0.45–2.25	0.2–1.75	—
Peak [O_2] (μmol L^{-1})	—	182–399	—	—
J_{SWI} (mmol O_2 m^{-2} h^{-1})	−0.05±0.04	0.03±0.04	−0.05±0.07	—
NPP (mmol O_2 m^{-2} h^{-1})	—	0.07±0.05	—	—
GPP (mmol O_2 m^{-2} h^{-1})	—	0.11±0.05	—	—
pH_{min}	7.74	7.69	7.68	—
pH_{max}	8.26	8.34	8.21	—

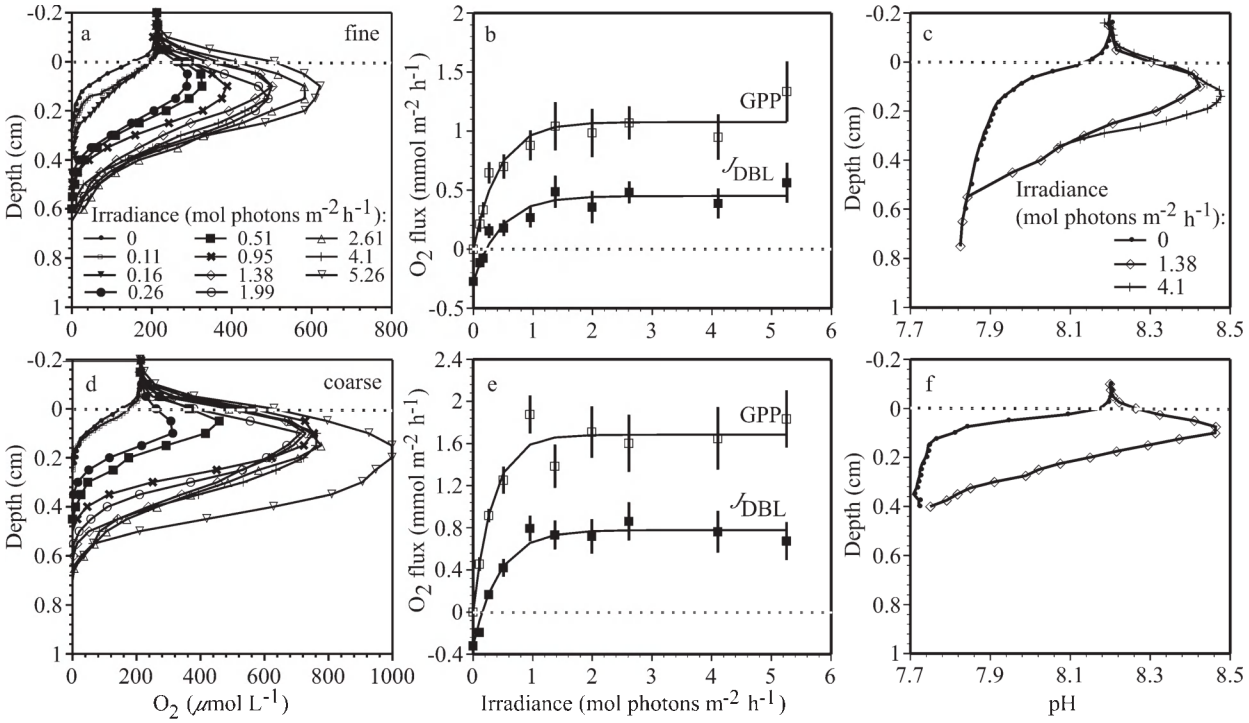

Fig. 7. Ex situ microsensor measurements in (a–c) fine and (d–f) coarse Heron Reef sands. (a, d) Steady-state O_2 profiles measured at various incident light intensities, as indicated in the legend. (b, e) Calculated gross photosynthesis rates and DBL O_2 fluxes (J_{DBL}) as a function of incident light intensity, with symbols representing the mean ± 1 SD of replicate measurements. Lines denote the best fit obtained with the inverted exponential model of Webb et al. (1974). (c, f) pH profiles measured in the dark and at saturating incident light intensities (*see* legend).

especially at site CS. The depletion of pore-water nutrient concentrations by advective exchange has been demonstrated in sediment core incubations reported by Jahnke et al. (2005). These patterns are all consistent with a strong influence of advective pore-water exchange in Heron Reef sands and its dependence on surface-water hydrodynamics and sediment permeability (Huettel and Webster 2001).

Benthic community metabolism—Photosynthesis in coastal sediments has long been known to depend on sediment PAR flux, leading to empirical parameterizations of benthic primary production dependent only on one variable, benthic light flux or water depth (Gattuso et al. 2006). Our laboratory microsensor measurements, conducted in steady-state diffusive conditions, confirm that the photosynthetic activity of microphytobenthos at Heron Reef exhibits the expected light-saturating behavior (Webb et al. 1974), although with light acclimation intensities (E_k; Table 4) that are lower than those previously observed in shallow tropical environments (Underwood 2002). Light intensity at the SWI during the daytime generally exceeds these measured acclimation intensities (Fig. 3), so based on

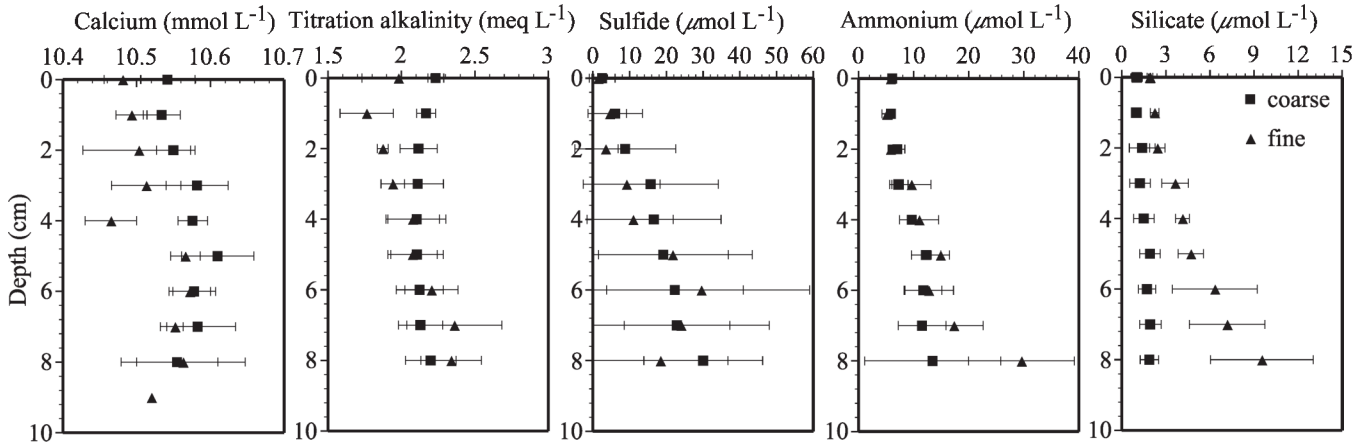

Fig. 8. Profiles of pore-water solutes in Heron Reef sediments. Symbols represent the mean ± 1 SD of replicate profiles of calcium (fine: $n = 3$; coarse: $n = 5$), TA ($n = 3$), sulfide ($n = 6$), ammonium, and silicate ($n = 3$).

our ex situ measurements made under diffusive conditions, one would expect that microphytobenthic primary productivity during most of the day would not be light-limited.

Our flux chamber results allow us to assess the influence of an additional factor, pore-water exchange, on benthic photosynthesis rates. For this purpose, we derived a multiple regression (Fig. 9) relating GPP to the independent variables pore-water filtration rate (FR) and benthic PAR exposure. The standardized partial regression coefficients (β), obtained by multiplying each regression coefficient by the ratio of SDs of independent and dependent variables, facilitate the direct comparison of the predictive power of each independent variable ($\beta_{PAR} = 0.57$ and $\beta_{FR} = 0.30$). The high value of β_{PAR} indicates an important link between microphytobenthic primary production and benthic light flux under in situ advective conditions indicative of light limitation, contrary to our expectations based on laboratory measurements under diffusive conditions. Furthermore, by removing the filtration rate, the variable with the smallest β coefficient, we observe that the correlation coefficient R decreases from 0.52 ($p = 0.03$) to 0.31 ($p < 0.0001$). This indicates that pore-water exchange adds considerable predictive capacity to the overall relationship and may therefore be valuable in integrating empirical and mechanistic parameterizations of benthic photosynthesis in coastal sediment biogeochemical and ecosystem models. Other factors may also have significant bearing on benthic photosynthesis, including differences in physical sediment properties (Table 1) and/or light penetration.

The influence of advective pore-water exchange on benthic primary production is further supported by the observation of higher O_2 fluxes (NPP; Table 3) in light chambers under advective conditions than under ex situ steady-state diffusive conditions at saturating illumination (J_{DBL}; Table 4). The difference between benthic photosynthesis rates measured in advective conditions with in situ flux chambers and ex situ rates under diffusive conditions indicates that pore-water advection relieves an important limitation of microphytobenthic productivity. The low nutrient [NH_4^+, NO_3^-, PO_4^{3-}, and $Si(OH)_4$] concentrations in both overlying water and pore water indicate nutrient limitation of benthic photosynthesis. Moreover, the near-zero nutrient [NH_4^+, NO_3^-, PO_4^{3-}, and $Si(OH)_4$] fluxes measured in light and dark chambers (data not shown) indicate tight nutrient recycling and a microphytobenthic community that is capable of storing nutrients (Longphuirt et al. 2009). However, it has been shown that under nutrient-limiting conditions, photosynthesis by benthic diatoms continues unbalanced, with overflow metabolism shunted to exopolysaccharide (EPS) excretion (Alcoverro et al. 2000). Hence, nutrient limitation may not be the only explanation for the observed dependence of NPP on advective exchange. Cook and Røy (2006) have suggested that the relief of CO_2 limitation could be a likely cause for enhanced microphytobenthic activity under advective conditions. Whatever factor may be limiting benthic photosynthesis in Heron Reef sands, reduced advective supply of the limiting factor under diffusive ex situ conditions likely explains the lower primary production rates and the reduced importance of light, as indicated by the low light-saturation intensities observed in the laboratory. Our results demonstrate that pore-water advection can, to some extent, alleviate nutrient limitation and promote co-limited production (light and nutrient limitation).

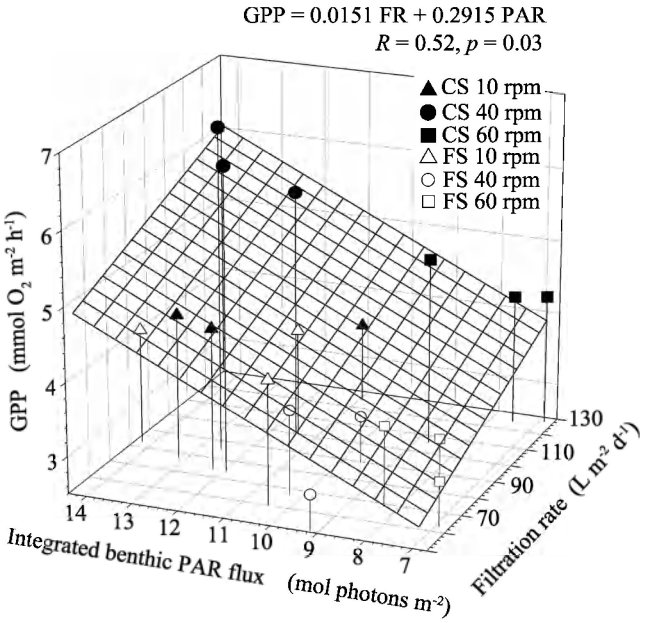

Fig. 9. Gross benthic primary production rate plotted as a function of pore-water filtration rate and integrated sediment light flux in individual light-chamber incubations. Individual incubations are denoted by sampling site (CS and FS: coarse sand and fine sand, respectively) and chamber stirring rate (10, 40, and 60 rpm). Regression coefficients and multivariate regression analysis are discussed in the text.

TOU in dark chambers was significantly enhanced by pore-water advection. The quantitative effect of advection on TOU can be estimated by comparing dark-chamber O_2 fluxes with DOU rates. This kind of comparison must be viewed with caution, however, because it has been shown that daytime dark-chamber O_2 fluxes may be more than a factor of 2 greater than nighttime O_2 fluxes (Jahnke et al. 2000). With this caveat in mind, flux chamber TOU has been compared with maximum DOU rates calculated from in situ nighttime O_2 microprofiles (0.19 and 0.15 mmol m^{-2} h^{-1} in CS and FS, respectively), yielding enhancements of TOU in flux chambers by factors of 8–14 and 6–9 in CS and FS, respectively. Flux chamber TOU can also be compared to J_{DBL} derived from diffusive ex situ O_2 microprofiles measured in the dark (Table 4), yielding enhancements of TOU in flux chambers by factors of 5–8 and 3–5 in CS and FS, respectively. Note that these factors are conservative, as pore-water flushing deepens in situ O_2 penetration and therefore reduces vertical gradients and DOU. The observed stimulation of TOU by pore-water advection is in agreement with previous observations in nearshore environments (Reimers et al. 2004). This effect is presumed to result from increased rates of aerobic respiration, nitrification, and/or sulfide oxidation in microenvironments and deeper layers of sediment due to greater penetration of dissolved O_2 in the presence of pore-water advection.

Table 5. Summary of daily O_2 and TA flux estimates (mean ± 1 SD) from replicate in situ light and dark benthic flux chamber incubations. Chamber sets are denoted by sampling site (CS and FS) and flux chamber stirring rate (10, 40, and 60 rpm).

mmol m^{-2} d^{-1}	O_2 flux	TA flux
CS 10 rpm		
Day	21.42±4.11	−18.41±2.60
Night	−24.03±3.15	26.63±8.00
Total	−2.61±5.17	8.22±8.41
CS 40 rpm		
Day	33.95±4.40	−21.34±3.87
Night	−35.58±5.02	22.52±6.38
Total	−1.62±6.68	1.19±7.46
CS 60 rpm		
Day	15.67±3.60	−13.98±7.69
Night	−41.06±1.65	8.66±12.74
Total	−25.39±3.96	−5.32±14.87
FS 10 rpm		
Day	25.88±0.96	−12.55±3.87
Night	−13.80±2.10	16.48±7.88
Total	12.07±2.31	3.93±8.77
FS 40 rpm		
Day	17.51±2.85	−5.56±3.82
Night	−17.42±5.60	33.15±1.48
Total	0.10±6.28	27.60±4.10
FS 60 rpm		
Day	15.92±1.90	−5.43±1.93
Night	−21.20±6.40	16.59±8.00
Total	−5.28±6.68	11.16±8.23

In addition to the enhanced dissolved O_2 supply, intruding bottom water also provides POM to permeable sediments, as suspended particles become trapped in the sediment matrix. This 'biocatalytic filter' effect (Huettel and Webster 2001), as well as spatial variability in macrofaunal activity, could provide an alternative explanation for the greater magnitude and variability of OCR and chamber-derived TOU observed in coarser sand (Fig. 4; Table 3). It should be noted, however, that areal OCR (FS: 3.54 mmol O_2 m^{-2} h^{-1}, CS: 6.77 mmol O_2 m^{-2} h^{-1}), calculated by multiplying the average OPD from nighttime in situ O_2 profiles (Fig. 6) by the average OCR measured in the oxic layer by planar optode (Fig. 4), are about three times greater than dark-chamber TOU estimates (Table 3). One possible explanation for this discrepancy is the dependence of O_2 consumption kinetics associated with microbial respiration, nitrification, and sulfide oxidation on O_2 concentration (Koch 1998). Since pore-water O_2 concentrations are enhanced by rapid percolation with air-saturated seawater in OCR imaging, potential OCR measured by the flow-through method of Polerecky et al. (2005) may be higher than in situ rates. However, because of the low saturation constant of O_2 in aerobic remineralization (Van Frausum et al. 2010), it is unlikely that this can entirely account for the difference between planar optode and flux chamber measurements of sediment O_2 consumption.

The greater Chl *a* content observed in coarser sediment (Fig. 2b) may be due to enhanced and deeper filtration of bottom water and suspended phytoplankton detritus through higher permeability sediment. Alternatively, this observation may be indicative of the effect of enhanced advective transport in stimulating benthic primary production in coarser sediment. Either way, the chlorophyll enrichment observed in coarser sediment is consistent with independent measurements indicating a higher metabolic activity in coarser sand.

Mean daily O_2 fluxes (Table 5) show a significant dependence on both filtration rate ($p = 0.0100$) and PAR flux ($p = 0.0141$), as shown in Table 2. The strength of this overall correlation ($R = 0.91$, $p = 0.0116$) shows that sediment PAR flux and pore-water filtration rates exert an important influence not only on rates of benthic respiration and gross photosynthesis but also on daily O_2 fluxes and the balance between autotrophy and heterotrophy in Heron Reef sediments as well. Interestingly, the predictive power of pore-water filtration is nearly as strong as that of benthic PAR flux on the parameterization of daily benthic O_2 fluxes ($\beta_{FR} = -0.60$, $\beta_{PAR} = 0.61$), while it is only about half as important as benthic PAR flux in estimating GPP, as discussed above.

Benthic $CaCO_3$ cycling—The uptake of CO_2 by benthic microalgae produces a small peak in pore-water pH and elevates the saturation state with respect to aragonite, promoting calcification at 1–2-mm depth (Figs. 6, 7). Several genera of coralline algae, benthic foraminifera, mollusks, and other organisms previously reported in Heron Reef sands may be responsible for calcification in surface sediments and the observed surficial dip in pore-water Ca^{2+} and TA (Fig. 8; Maiklem 1968). Below the surface layer, CO_2 release by oxic respiration and acidity generated by sulfide oxidation result in lower pore-water pH and Ω_a (Figs. 6, 7), promoting Ca^{2+} and TA release by $CaCO_3$ dissolution around 5 cm depth (Fig. 8). Further TA release by sulfate reduction in deeper sediments probably contributes to higher Ω_a at depth, precluding further dissolution (Fig. 8).

We first interpret calculated pore-water Ω_a profiles (Fig. 6) in the context of a conceptual sediment model, in which the decrease in advective pore-water velocities with depth leads to a vertical zonation of $CaCO_3$ dynamics in the sediment. In surface sediments, photosynthetically induced supersaturation and rapid advective transport provide an efficient supply of Ca^{2+} and dissolved inorganic carbon (DIC) for calcification, which therefore proceeds at rates limited only by the catalysis of $CaCO_3$ precipitation at the cell or mineral surface (rate limitation). In deeper sediments, solute exchange is slower, and pore-water Ω_a is expected to approach values slightly below 1, to maintain a dynamic equilibrium between aragonite dissolution and calcite precipitation, which should proceed according to the rate of transport of Ca^{2+} and carbonate species in the pore water (transport limitation). However, Ω_a appears to approach values greater than 1 at depth (Fig. 6). On face value, this would rule out $CaCO_3$ dissolution, despite measurable Ca^{2+} and TA effluxes in dark chambers. Some

variability in Ω_a may be explained by the choice of carbonic and boric acid dissociation constants (Gehlen et al. 2005). It is also important to recognize that the in situ pH and TA profiles used to calculate Ω_a profiles have a different vertical resolution and were not measured simultaneously in time or space. For these reasons, calculated Ω_a profiles must be viewed with caution. Despite these sources of variability, we indeed expect that deviations from equilibrium in deeper sediments should be far less pronounced than they are near the SWI, where pore-water advection relieves transport limitation and favors rate-limited $CaCO_3$ dynamics with pore-water solute concentrations far from equilibrium. Indeed, undersaturated conditions may occur only locally at depth as a result of remineralization hotspots or on short timescales following disturbances, when temporary buildup of Ca^{2+} and TA in deeper pore water may be flushed out by deep mixing.

To examine the effect of benthic calcification and $CaCO_3$ dissolution on flux chamber Ca^{2+} and alkalinity results, we first compare measured Ca^{2+} and TA fluxes in Fig. 10. Some scatter around the 2 : 1 ratio is expected, simply because of the analytical challenge associated with precise small volume titrations for TA and especially Ca^{2+}, against the high seawater background. The Ca^{2+} fluxes follow TA fluxes reasonably well, with the exception of one light-chamber incubation in FS at 40 rpm. This incubation displayed an anomalously high Ca^{2+} flux out of the sediment, higher even than any measured dark-chamber Ca^{2+} efflux. Therefore, the results of this incubation should be interpreted with care. Overall, our results are not significantly different from the expected ratio of 2 : 1, with a mean ratio of 2.69 (Wilcoxon; $p = 0.22$; $\mu = 2$), indicating that measured benthic Ca^{2+} and TA fluxes are mainly controlled by $CaCO_3$ dissolution and precipitation in Heron Reef sediments. The high average TA : Ca^{2+} flux ratio might be due to preferential dissolution of the more soluble aragonite and high-Mg calcite phases and precipitation of less soluble low-Mg calcite in reducing sediments. This explanation is consistent with the observation of a large HMC fraction and a small LMC fraction in Heron Reef sands (Table 1). However, there is no detectable variation in the depth distribution of these two fractions to support this explanation, probably because of rapid sediment transport under high energy conditions. In the following discussion, we use TA flux as a measure of calcification and $CaCO_3$ dissolution.

Significant TA consumption was measured in all light-chamber incubations, indicative of benthic calcification. Without further study, we cannot determine the relative importance of biotic and abiotic processes on calcification in Heron sands. However, we can add anecdotally that we observed reddish grains in both FS and CS, indicating the presence of active crustose coralline algae, which are known to form calcareous pavements on the reef edge (Maiklem 1968). Other calcification mechanisms may also be present. For example, it has been proposed that EPS may promote calcification by binding Ca^{2+} and providing nucleation sites as well as by releasing Ca^{2+} and therefore elevating the pore-water saturation state upon EPS remineralization (Decho et al. 2005). However, testing this

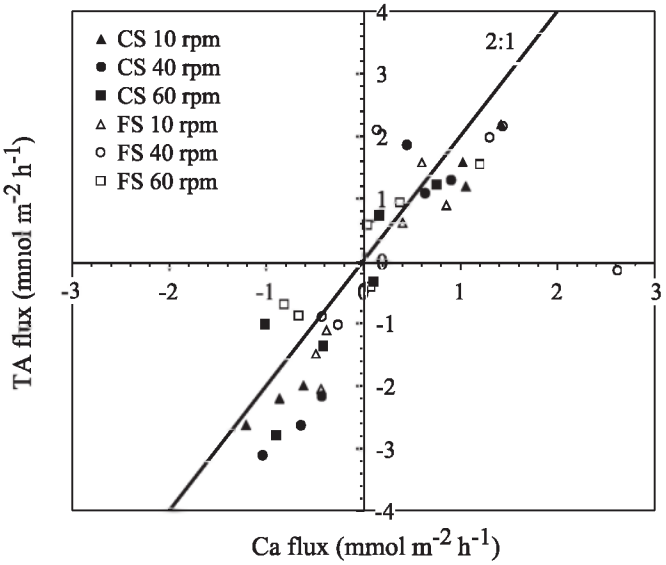

Fig. 10. Summary of TA vs. calcium flux for all light- and dark-chamber incubations. Individual incubations are denoted by sampling site (CS and FS: coarse sand and fine sand, respectively) and flux chamber stirring rate (10, 40, and 60 rpm). The 2 : 1 line is indicated for reference.

hypothesis is beyond the scope of the current study. Multiple regression analysis (Fig. 11) of light-chamber TA flux and the independent variables pore-water filtration rate and NPP indicates that benthic photosynthesis is the dominant control on calcification ($\beta_{NPP} = -0.37$ and $\beta_{FR} = -0.19$). This conclusion is in agreement with the results of a recent study by Werner et al. (2008) based on O_2, pH, and Ca^{2+} microprofiles and with the prevailing view that benthic phototrophic communities enhance calcification by removing CO_2 and thereby increasing the pore-water carbonate saturation state (Schoon et al. 2010).

Interestingly, by again removing the least effective independent variable (filtration rate), it becomes apparent that this variable adds predictive capacity to the regression (R decreases from 0.59 [$p = 0.0093$] to 0.50 [$p = 0.03$]). This stimulation of net calcification by pore-water advection in the light is unexpected and may be explained by a deepening of surface supersaturation as bottom water and euphotic-zone pore water are flushed into deeper sediments (compare Figs. 6 and 7). Alternately, it may result from the role of pore-water advection in supplying Ca^{2+} and DIC for calcification and/or in stimulating benthic photosynthesis and therefore pore-water supersaturation in surface sediments. Whatever the reason, this intriguing influence of pore-water advection on benthic calcification requires further investigation.

In dark chambers, one might expect a direct relation between net $CaCO_3$ dissolution and net respiration rates due to the release of metabolic acidity in sediments. However, this effect is not apparent, and there is no direct relation between TA efflux and TOU in dark chambers (Spearman; $p = 0.57$). This observation may be explained, at least in part, by the effect of pore-water advection on the efficiency of metabolic $CaCO_3$ dissolution. Here, metabolic

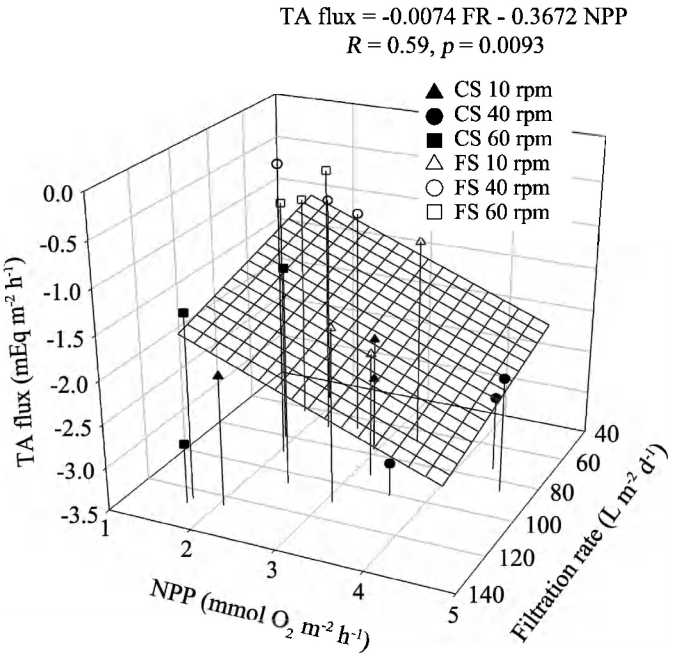

Fig. 11. Calcification rate (TA flux) in the light as a function of net benthic primary production (O_2 flux) and filtration rate in fine and coarse carbonate sands. Symbols indicate individual flux chamber incubations conducted at different stirring speeds in fine and coarse sand. Regression coefficients and multivariate regression analysis are discussed in the text.

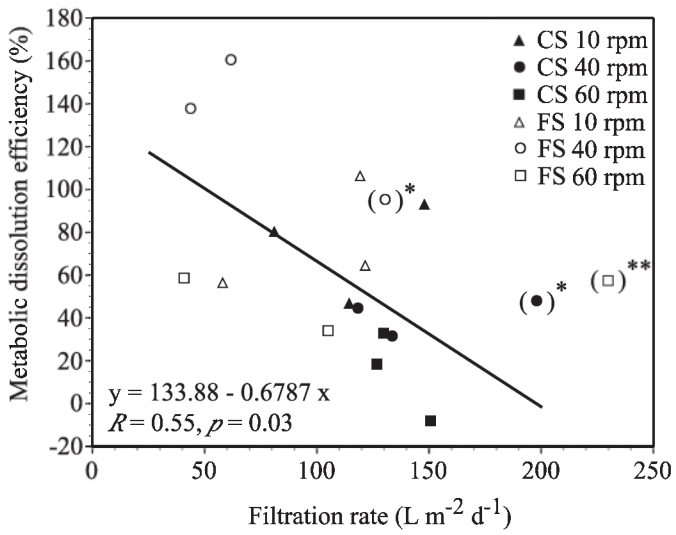

Fig. 12. Relationship between metabolic dissolution efficiency (ξ) and filtration rate in dark-chamber incubations in fine and coarse carbonate sand. Metabolic dissolution efficiency is calculated as explained in the text. Symbols indicate individual flux chamber measurements conducted at different stirring speeds in fine and coarse sand. Parentheses denote incubations in which measured filtration rates were significantly higher than the mean in each set of six chambers (Grubb's outlier test; ** $p < 0.05$; * $p < 0.10$), most likely as a result of the irrigation activity of macroinfauna. These outliers are not included in the trend line.

dissolution efficiency (ξ) is represented by the ratio of the net $CaCO_3$ dissolution rate to the remineralization rate of organic carbon. In dark chambers, net $CaCO_3$ dissolution rate is calculated as half of the chamber TA flux, and the respiration rate is calculated from dark-chamber O_2 flux using a respiratory quotient of 0.77 and therefore assuming that the oxidation of organic matter of Redfield composition releases CO_2 and NO_3^-. As the fraction of respiratory CO_2 and metabolic acidity contributing to $CaCO_3$ dissolution varies from 0 to 1, ξ is expected to increase from 0% to 100%. In Fig. 12, the metabolic dissolution efficiency is presented as a function of filtration rate. In Heron Reef sands, the value of this ratio falls from unity at low filtration rates to less than zero at the highest filtration rates. If we exclude the three incubations with anomalously high filtration rates, as discussed in the "Advective pore-water exchange" section, this correlation becomes statistically significant (Fig. 12), confirming that the damping effect of pore-water filtration on the efficiency of respiration-driven dissolution in carbonate sands is a robust observation. The observed effect of pore-water exchange on metabolic dissolution efficiency can be explained by the enhanced influx of supersaturated bottom water and/or loss of metabolic acidity under increased filtration. This limits the effect of aerobic respiration and sulfide oxidation on lowering pore-water saturation state and promoting carbonate dissolution.

Estimates of benthic TA flux in CS and FS scaled on a per-day basis demonstrate the significance of net $CaCO_3$ dissolution in Heron Reef deposits in all but the highest energy conditions (60 rpm) in CS when we observed net calcification (Tables 2, 5). The variability in integrated daily TA flux can be explained in large part by the influence of pore-water advection (Spearman; $p = 0.03$), in general agreement with the effects observed in both light- and dark-chamber results (Figs. 11, 12). However, these conclusions are tempered by substantial variability in sediment characteristics, microalgal communities, and pore-water filtration rates and mechanisms. Several seasonally variable factors, such as daily insolation, temperature, organic matter loading, wave height, current velocity, and storm events, will also influence daily TA flux. Clearly, more measurements are necessary to accurately trace the seasonal and spatial variability in $CaCO_3$ cycling in Heron Reef deposits, with its wide distribution of grain size and sorting (Maxwell et al. 1964). Nevertheless, our results illustrate the potential role of advective pore-water exchange on daily $CaCO_3$ dynamics in permeable sediments. Strikingly, rapid pore-water advection has the potential to reverse the net $CaCO_3$ balance and promote $CaCO_3$ preservation in permeable biogenic deposits, as we observed in chamber incubations in CS under rapid stirring (60 rpm). By inference, pore-water filtration may have profound implications on ecosystem carbon budgets in reef environments, mediating the role of sediments in buffering changes in surface-water saturation state due to the recycling of natural POM and whole reef calcification. Considering previous measurements of pore-water advective velocities in natural sediments of similar permeability that can be 1 to 2 orders of magnitude greater than the flushing rates measured in this study (Reimers et al. 2004), considerable temporal and spatial variability in net benthic carbonate budgets are expected.

Implications for Heron Reef and global ocean $CaCO_3$ cycling—Our results confirm previous observations of extremely rapid benthic primary production and organic matter turnover rates in permeable biogenic deposits at Heron Reef (Wild et al. 2004; Werner et al. 2006). The net sediment trophic status was found to depend on both benthic light flux and pore-water filtration rate, through their combined influence on benthic microalgal photosynthesis and sediment community respiration.

Benthic photosynthesis promotes calcification, and respiration induces metabolic $CaCO_3$ dissolution in Heron Reef sediments. The results presented in this study indicate that pore-water advection exerts a considerable influence on calcification, the efficiency of respiration-driven $CaCO_3$ dissolution, net alkalinity fluxes, and the net $CaCO_3$ budget in permeable sediments. These observations (Figs. 11, 12) serve to amplify the previously reported effects of surface sediment calcification and elevated organic matter deposition on reducing metabolic dissolution efficiency in ocean margin sediments, where permeable sands with pressure-induced advective transport are prevalent (Huettel and Webster 2001). Calcification at the SWI intensifies in shallower water as a result of increasing seawater supersaturation and photosynthesis by benthic microalgae in ocean margin sediments within the euphotic zone (Werner et al. 2008; Schoon et al. 2010), counteracting metabolic dissolution. The rapid escape of metabolic acidity from sediment pore water to the overlying water is also favored closer to shore, where remineralization length scales are reduced as a result of greater availability of labile organic matter (Martin and Sayles 2006). All of these mechanisms therefore favor less efficient metabolic dissolution in ocean margin sediments than in the deep sea. We conclude that accurate models of the past, present, and future ocean carbonate system should include a depth-dependent parameterization of respiration-driven $CaCO_3$ dissolution in sediments in order to better represent our current mechanistic understanding of benthic $CaCO_3$ dynamics.

The results of the present study demonstrate that biogenic carbonate sediments at Heron Reef generally undergo net dissolution on a daily basis, although $CaCO_3$ preservation is favored by stronger pore-water advection driven by the most energetic hydrodynamic conditions (Table 5). This conclusion differs markedly from reports that these sediments may be net calcifying, based on studies conducted under diffusive conditions (Werner et al. 2008; Schoon et al. 2010). Indeed, under strictly diffusive conditions, benthic Ca^{2+} and TA influxes would result from negative solute concentration gradients in the diffusive boundary layer, where calcification dominates as a result of high Ω, as shown in Figs. 6 and 8 and in earlier microsensor studies. However, such transport-limited conditions are not the norm in permeable biogenic reef sediments, where pore-water exchange is enhanced by wave and tidal pumping, bottom currents over sediment topography, and bioirrigation (Huettel and Webster 2001). Under natural conditions, pore-water advection activates exchange with deeper sediment layers, where metabolic acidity is neutralized by $CaCO_3$ dissolution, as discussed in the previous section.

Does net dissolution of $CaCO_3$ in reef sediments constitute a relevant sink on the scale of annual coral reef growth? Ryan et al. (2001) have estimated an average present-day $CaCO_3$ production rate ($G = 3.1$ kg $CaCO_3$ m^{-2} yr^{-1}) for neighboring Wistari Reef based on the classification of reef top biogeographical zones using ground-truthed remote sensing data and earlier measurements of G using the alkalinity anomaly approach (Smith and Key 1975) in different zones. If we assume a similar production rate over a reef area of 27.8 km^2, then an estimated annual $CaCO_3$ production rate of 8.6×10^7 kg yr^{-1} is obtained for Heron Reef.

To the best of our knowledge, precise estimates of areal sediment coverage in the above-mentioned physiographic regions at Heron Reef have never been reported. Nevertheless, a 'back-of-the-envelope' estimate can be achieved from the detailed study of Maxwell et al. (1964), who described the full range of faunal densities, from a "profusion of living coral [~ 100% coral cover]" at the reef edge to a section of the lagoon where "there is a noticeable absence of large coral growth [~ 0% coral cover]." Within this wide range lie the remaining lagoon area and the reef flat, with approximately 50% and 75% sediment cover, respectively. Given these constraints, a total reef top sediment area of 17.9 km^2 is estimated. Using mean light- and dark-chamber alkalinity fluxes and assuming an annual average 8.4 h d^{-1} of sunshine (http://www.bom.gov.au/climate/averages/tables/cw_039122.shtml), we calculate that approximately 2.3×10^6 kg of $CaCO_3$ dissolves in Heron Reef sediments annually, representing only 2.7% of annual reef top production. While net dissolution of $CaCO_3$ in reef sediments represents a very small fraction of reef top production at Heron Reef today, recent studies (Anderson et al. 2009) indicate that some reef ecosystems may begin to experience a net loss of $CaCO_3$ within this century, as a result of anthropogenic CO_2 emissions.

Acknowledgments

We thank the Max Planck Institute Microsensor, Nutrient, and Habitat Group technicians and Stella Nemecky for technical and analytical support. We also acknowledge V. Meyer, P. Färber, H. Osmers, and F. Janssen for assistance in the preparation and use of field equipment. C. Y. Robertson (SkIO), N. Fagel (U. Liège), and S. Bertrand (U. Ghent) provided access to instrumentation for microtitration, x-ray diffraction, and grain size analyses. Field sampling was conducted under permit G10/33177.1 of the Great Barrier Reef Marine Park Authority. The staff of the Heron Island Research Station were instrumental in promoting an enjoyable and productive field campaign. The manuscript benefited from numerous helpful comments provided by the Associate Editor, R. Glud, and two anonymous reviewers. This study was supported by the Max Planck Society (M.P.G.), an Alexander von Humboldt postdoctoral fellowship (A.R.), an Odysseus grant from the Research Foundation–Flanders (F.J.R.M.), and a Vidi grant from the Netherlands Organization for Scientific Research (F.J.R.M.).

References

Alcoverro, T., E. Conte, and L. Mazzella. 2000. Production of mucilage by the Adriatic epipelic diatom *Cylindrotheca closterium* (Bacillariophyceae) under nutrient limitation. J. Phycol. **36:** 1087–1095, doi:10.1046/j.1529-8817.2000.99193.x

Alongi, D. M., J. Pfitzner, and L. A. Trott. 2006. Deposition and cycling of carbon and nitrogen in carbonate mud of the lagoons of Arlington and Sudbury Reefs, Great Barrier Reef. Coral Reefs **25:** 123–143, doi:10.1007/s00338-005-0069-2

Anderson, A. J., I. B. Kuffner, F. T. Mackenzie, P. L. Jokiel, K. S. Rodgers, and A. Tan. 2009. Net loss of $CaCO_3$ from a subtropical calcifying community due to seawater acidification: Mesocosm-scale experimental evidence. Biogeoscience **6:** 1811–1823, doi:10.5194/bg-6-1811-2009

Archer, D. 1996. A data-driven model of the global calcite lysocline. Glob. Biogeochem. Cycles **10:** 511–526, doi:10.1029/96GB01521

Bender, M., R. Jahnke, R. Weiss, W. Martin, D. Heggie, J. Orchardo, and T. Sowers. 1989. Organic carbon oxidation and benthic nitrogen and silica dynamics in San Clemente Basin, a continental borderland site. Geochim. Cosmochim. Acta **53:** 685–697, doi:10.1016/0016-7037(89)90011-2

Boudreau, B. P. 1997. Diagenetic models and their implementation. Springer.

———, J. J. Middelburg, and F. J. R. Meysman. 2010. Carbonate compensation dynamics. Geophys. Res. Lett. **37:** L03603, doi:10.1029/2009GL041847

Brindley, G. W., and G. Brown. 1980. Crystal structures of clay minerals and their X-ray identification. Mineralogical Society Monograph No. 5. Mineralogical Society.

Broecker, W. S., and T.-H. Peng. 1987. The role of $CaCO_3$ compensation in the glacial to interglacial atmospheric CO_2 change. Glob. Biogeochem. Cycles **1:** 215–239.

Burdige, D. J., and R. C. Zimmerman. 2002. Impact of sea grass density on carbonate dissolution in Bahamian sediments. Limnol. Oceanogr. **47:** 1751–1763, doi:10.4319/lo.2002.47.6.1751

Cline, J. D. 1969. Spectrophotometric determination of hydrogen sulfide in natural waters. Limnol. Oceanogr. **14:** 454–458, doi:10.4319/lo.1969.14.3.0454

Cook, H., P. Johnson, J. Matti, and I. Zemmels. 1975. Methods of sample preparation and x-ray diffraction data analysis, x-ray mineralogy laboratory, deep sea drilling project, University of California, Riverside, p. 999–1007. *In* A. G. Kaneps [ed.], Initial reports of the deep sea drilling project version 28. U.S. Government Printing Office.

Cook, P. L. M., and H. Røy. 2006. Advective relief of CO_2 limitation in microphytobenthos in highly productive sandy sediments. Limnol. Oceanogr. **51:** 1594–1601, doi:10.4319/lo.2006.51.4.1594

Decho, A. W., P. T. Visscher, and R. P. Reid. 2005. Production and cycling of natural microbial exopolymers (EPS) within a marine stromatolite. Palaeogeogr. Palaeoclimatol. **219:** 71–86, doi:10.1016/j.palaeo.2004.10.015

Dickson, A. G. 1990. Thermodynamics of the dissociation of boric acid in synthetic seawater from 273.15 to 318.15K. Deep-Sea Res. **37:** 755–766.

———, and F. J. Millero. 1987. A comparison of the equilibrium constants for the dissociation of carbonic acid in seawater media. Deep-Sea Res. **34:** 1733–1743.

Emery, K. O. 1968. Relict sediments on continental shelves of the world. Am. Assoc. Petrol. Geol. Bull. **52:** 445–464.

Flügel, E. 2004. Microfacies analysis of carbonate rocks. Springer-Verlag.

Forster, S., and G. Graf. 1995. Impact of irrigation on oxygen flux into the sediment: Intermittent pumping by *Callianassa subterranea* and 'piston-pumping' by *Lanice conchilega*. Mar. Biol. **123:** 335–346, doi:10.1007/BF00353625

Gattuso, J. P., B. Gentilli, C. Duarte, J. Kleypas, J. J. Middelburg, and D. Antoine. 2006. Light availability in the coastal ocean: Impact on the distribution of benthic photosynthetic organism and contribution to primary production. Biogeoscience **3:** 489–513, doi:10.5194/bg-3-489-2006

Gehlen, M., F. C. Bassinot, L. Chou, and D. McCorkle. 2005. Reassessing the dissolution of marine carbonates. Part I: Solubility. Deep-Sea Res. I **52:** 1445–1460, doi:10.1016/j.dsr.2005.03.010

Glud, R. N., S. Forster, and M. Huettel. 1996. Influence of radial pressure gradients on solute exchange in stirred benthic chambers. Mar. Ecol. Prog. Ser. **141:** 303–311, doi:10.3354/meps141303

———, J. K. Gundersen, and O. Holby. 1999. Benthic in situ respiration in the upwelling area off central Chile. Mar. Ecol. Prog. Ser. **186:** 9–18, doi:10.3354/meps186009

Guinotte, J. M., and V. J. Fabry. 2008. Ocean acidification and its potential effects on marine ecosystems, p. 320–342. *In* R. S. Ostfeld and W. H. Schlesinger [eds.], The year in ecology and conservation biology 2008. Annals of the New York Academy of Sciences.

Holst, G., and B. Grunwald. 2001. Luminescence lifetime imaging with transparent oxygen optodes. Sens. Actuat. B-Chem. **74:** 78–90, doi:10.1016/S0925-4005(00)00715-2

Huettel, M., and I. T. Webster. 2001. Porewater flow in permeable sediment, p. 144–179. *In* B. P. Boudreau and B. B. Jørgensen [eds.], The benthic boundary layer: Transport processes and biogeochemistry. Oxford Univ. Press.

Jahnke, R. A. 1996. The global ocean flux of particulate organic carbon: Areal distribution and magnitude. Glob. Biogeochem. Cycles **10:** 71–88, doi:10.1029/95GB03525

———, and D. B. Jahnke. 2000. Rates of C, N, P and Si recycling and denitrification at the US Mid-Atlantic continental slope depocenter. Deep-Sea Res. I **47:** 1405–1428, doi:10.1016/S0967-0637(99)00118-1

———, and ———. 2004. Calcium carbonate dissolution in deep sea sediments: Reconciling microelectrode, pore water and benthic flux chamber results. Geochim. Cosmochim. Acta **68:** 47–59, doi:10.1016/S0016-7037(03)00260-6

———, J. R. Nelson, R. L. Marinelli, and J. E. Eckman. 2000. Benthic flux of biogenic elements on the southeastern US continental shelf: Influence of pore water advective transport and benthic microalgae. Cont. Shelf Res. **20:** 109–127, doi:10.1016/S0278-4343(99)00063-1

———, M. Richards, J. Nelson, C. Robertson, A. Rao, and D. Jahnke. 2005. Organic matter remineralization and porewater exchange rates in permeable South Atlantic Bight continental shelf sediments. Cont. Shelf Res. **25:** 1433–1452, doi:10.1016/j.csr.2005.04.002

Janssen, F., M. Huettel, and U. Witte. 2005. Pore-water advection and solute fluxes in permeable marine sediments (I): Calibration and performance of the novel benthic chamber system *Sandy*. Limnol. Oceanogr. **50:** 768–778, doi:10.4319/lo.2005.50.3.0768

Kana, T. M., C. Darkangelo, M. D. Hunt, J. B. Oldham, G. E. Bennett, and J. C. Cornwell. 1994. Membrane inlet mass spectrometer for rapid high-precision determination of N_2, O_2, and Ar in environmental water samples. Anal. Chem. **66:** 4166–4170, doi:10.1021/ac00095a009

Koch, A. L. 1998. The Monod model and its alternatives, p. 62–93. *In* A. L. Koch, J. A. Robinson, and G. A. Milliken [eds.], Mathematical modeling in microbial ecology. Chapman & Hall.

Kristensen, E. 2001. Impact of polychaetes (*Nereis* spp. and *Arenicola marina*) on carbon biogeochemistry in coastal marine sediment: A review. Geochem. Trans. **2:** 92–104, doi:10.1186/1467-4866-2-92

Li, Y.-H., and S. Gregory. 1974. Diffusion of ions in sea water and in deep-sea sediments. Geochim. Cosmochim. Acta **38:** 703–714, doi:10.1016/0016-7037(74)90145-8

Logan, D., K. A. Townsend, K. Townsend, and I. R. Tibbetts. 2008. Meiofauna sediment relations in leeward slope turf algae of Heron Island reef. Hydrobiologia **610:** 269–276, doi:10.1007/s10750-008-9442-9

Longphuirt, S. N., J. H. Lim, A. Leynaert, P. Claquin, E. J. Choy, C. K. Kang, and S. An. 2009. Dissolved inorganic nitrogen uptake by intertidal microphytobenthos: Nutrient concentrations, light availability and migration. Mar. Ecol. Prog. Ser. **379:** 33–44, doi:10.3354/meps07852

Lorenzen, C. J. 1967. Determination of chlorophyll and pheopigments: Spectrophotometric equations. Limnol. Oceanogr. **12:** 343–346, doi:10.4319/lo.1967.12.2.0343

Maiklem, W. R. 1968. The Capricorn reef complex, Great Barrier Reef, Australia. J. Sediment. Petrol. **38:** 785–798.

Martin, W. R., and F. L. Sayles. 2006. Organic matter oxidation in deep-sea sediments: Distribution in the sediment column and implications for calcite dissolution. Deep-Sea Res. II **53:** 771–792, doi:10.1016/j.dsr2.2006.01.017

Maxwell, W. G. H., J. S. Jell, and R. G. McKellar. 1964. Differentiation of carbonate sediments in the Heron Island reef. J. Sediment. Petrol. **34:** 294–308.

Mehrbach, C., C. H. Culberson, J. E. Hawley, and R. M. Pytkowicz. 1973. Measurement of the apparent dissociation constants of carbonic acid in seawater at atmospheric pressure. Limnol. Oceanogr. **18:** 897–907, doi:10.4319/lo.1973.18.6.0897

Mélières, F. 1978. X-ray mineralogy studies, Leg 41, Deep-sea drilling project, eastern North Atlantic Ocean, p. 1065–1086. *In* Y. Lancelot and others [eds.], Initial reports of the deep sea drilling project, version 41. U.S. Government Printing Office.

Milliman, J. D. 1974. Marine carbonates. Recent sedimentary carbonates. Part 1. Springer-Verlag.

———, and A. W. Droxler. 1996. Neritic and pelagic carbonate sedimentation in the marine environment: Ignorance is not bliss. Geol. Rundsch. **85:** 496–504, doi:10.1007/BF02369004

Mucci, A. 1983. The solubility of calcite and aragonite in seawater at various salinities, temperatures and one atmosphere total pressure. Am. J. Sci. **283:** 780–799, doi:10.2475/ajs.283.7.780

Polerecky, L., A. Bachar, R. Schoon, M. Grinstein, B. B. Jørgensen, D. de Beer, and H. M. Jonkers. 2007. Contribution of *Chloroflexus* respiration to oxygen cycling in a hypersaline microbial mat from Lake Chiprana, Spain. Environ. Microbiol. **9:** 2007–2024, doi:10.1111/j.1462-2920.2007.01317.x

———, U. Franke, U. Werner, B. Grunwald, and D. de Beer. 2005. High spatial resolution measurement of oxygen consumption rates in permeable sediments. Limnol. Oceanogr.: Methods **3:** 75–85, doi:10.4319/lom.2005.3.75

Presley, B. J. 1971. Techniques for analyzing interstitial water samples. Part I. Determination of selected minor and major inorganic constituents, p. 1749–1755. *In* E. L. Winterer and others [eds.], Initial reports of the deep sea drilling project, version 7. U.S. Government Printing Office.

Rao, A., M. J. McCarthy, W. S. Gardner, and R. A. Jahnke. 2007. Respiration and denitrification in permeable continental shelf deposits on the South Atlantic Bight: Rates of carbon and nitrogen cycling from sediment column experiments. Cont. Shelf Res. **27:** 1801–1819, doi:10.1016/j.csr.2007.03.001

Reimers, C. E., R. A. Jahnke, and L. Thomsen. 2001. In situ sampling in the benthic boundary layer, p. 245–268. *In* B. P. Boudreau and B. B. Jørgensen [eds.], The benthic boundary layer: Transport processes and biogeochemistry. Oxford Univ. Press.

———, and others. 2004. In situ measurements of advective solute transport in permeable shelf sands. Cont. Shelf Res. **24:** 183–201, doi:10.1016/j.csr.2003.10.005

Ryan, D., B. Opdyke, and J. Jell. 2001. Holocene sediments of Wistari Reef: Towards a global quantification of coral reef related neritic sedimentation in the Holocene. Palaeogeogr. Palaeoclimatol. **175:** 173–184, doi:10.1016/S0031-0182(01)00370-4

Santos, I. R., R. N. Glud, D. Maher, D. Erler, and B. D. Eyre. 2011. Diel coral reef acidification driven by porewater advection in permeable carbonate sands, Heron Island, Great Barrier Reef. Geophys. Res. Lett. **38:** L03604, doi:10.1029/2010GL046053

Schoon, R., A. Bissett, and D. de Beer. 2010. Resilience of porewater chemistry and calcification in photosynthetic zones of calcifying sediments. Limnol. Oceanogr. **55:** 377–385, doi:10.4319/lo.2010.55.1.0377

Seeberg-Elverfeldt, J., M. Schlüter, T. Feseker, and M. Kölling. 2005. Rhizon sampling of porewaters near the sediment-water interface of aquatic systems. Limnol. Oceanogr.: Methods **3:** 361–371, doi:10.4319/lom.2005.3.361

Smith, S. V., and G. S. Key. 1975. Carbon dioxide and metabolism in marine environments. Limnol. Oceanogr. **20:** 493–495, doi:10.4319/lo.1975.20.3.0493

Strickland, J. D. H., and T. R. Parsons. 1972. A practical handbook of seawater analysis. Fisheries Research Board of Canada.

Tsunogai, S., M. Nishimura, and S. Nakaya. 1968. Complexometric titration of calcium in the presence of larger amounts of magnesium. Talanta **15:** 385–390, doi:10.1016/0039-9140(68)80247-4

Underwood, G. J. C. 2002. Adaptations of tropical marine microphytobenthic assemblages along a gradient of light and nutrient availability in Suva Lagoon, Fiji. Eur. J. Phycol. **37:** 449–462, doi:10.1017/S0967026202003785

Van Frausum, J., J. J. Middelburg, K. Soetaert, and F. J. R. Meysman. 2010. Different proxies for the reactivity of aquatic sediments towards oxygen: A model assessment. Ecol. Model. **221:** 2054–2067, doi:10.1016/j.ecolmodel.2010.06.001

Walsh, J. J. 1991. Importance of continental margins in the marine biogeochemical cycling of carbon and nitrogen. Nature **350:** 53–55, doi:10.1038/350053a0

Webb, A. P., and B. D. Eyre. 2004. The effect of natural populations of the burrowing thalassinidean shrimp *Typaea australiensis* on sediment irrigation and benthic metabolism, nutrient fluxes and denitrification. Mar. Ecol. Prog. Ser. **268:** 205–220, doi:10.3354/meps268205

Webb, W. L., M. Newton, and D. Starr. 1974. Carbon dioxide exchange of *Alnus rubra*: A mathematical model. Oecologia **17:** 281–291, doi:10.1007/BF00345747

Weiss, R. F. 1970. Solubility of nitrogen, oxygen, and argon in water and seawater. Deep-Sea Res. **17:** 721–735.

Werner, U., and others. 2006. Spatial patterns of aerobic and anaerobic mineralization rates and oxygen penetration dynamics in coral reef sediments. Mar. Ecol. Prog. Ser. **309:** 93–105, doi:10.3354/meps309093

———, and ———. 2008. Microbial photosynthesis in coral reef sediments (Heron Reef, Australia). Estuar. Coast. Shelf Sci. **76:** 876–888, doi:10.1016/j.ecss.2007.08.015

Wild, C., M. Rasheed, C. Jantzen, P. Cook, U. Struck, M. Huettel, and A. Boetius. 2005. Benthic metabolism and degradation of natural particulate organic matter in carbonate and silicate reef sands of the northern Red Sea. Mar. Ecol. Prog. Ser. **298:** 69–78, doi:10.3354/meps298069

———, R. Tollrian, and M. Huettel. 2004. Rapid recycling of coral mass-spawning products in permeable reef sediments. Mar. Ecol. Prog. Ser. **271:** 159–166, doi:10.3354/meps271159

Associate editor: Ronnie Nøhr Glud

Received: 05 August 2011
Accepted: 29 January 2012
Amended: 06 February 2012